

Strong-coupling magnetophononics: Self-blocking, phonon-bitriplons, and spin-band engineeringM. Yarmohammadi ^{1,2,*}, M. Krebs ², G. S. Uhrig ² and B. Normand ^{3,4}¹*Department of Physics, The University of Texas at Dallas, Richardson, Texas 75080, USA*²*Condensed Matter Theory, Department of Physics, TU Dortmund University, Otto-Hahn-Straße 4, D-44221 Dortmund, Germany*³*Laboratory for Theoretical and Computational Physics, Paul Scherrer Institute, CH-5232 Villigen PSI, Switzerland*⁴*Institute of Physics, Ecole Polytechnique Fédérale de Lausanne (EPFL), CH-1015 Lausanne, Switzerland*

(Received 14 December 2021; revised 2 May 2023; accepted 3 May 2023; published 11 May 2023; corrected 17 August 2023)

Magnetophononics, the modulation of magnetic interactions by driving infrared-active lattice excitations, is emerging as a key mechanism for the ultrafast dynamical control of both semiclassical and quantum spin systems by coherent light. We demonstrate that, in a quantum magnet with strong spin-phonon coupling, resonances between the driven phonon and the spin excitation frequencies exhibit an intrinsic self-blocking effect, whereby only a fraction of the available laser power is absorbed by the phonon. Using the quantum master equations governing the nonequilibrium steady states of the coupled spin-lattice system, we show how self-blocking arises from the self-consistent alteration of the resonance frequencies. We link this to the appearance of mutually repelling collective spin-phonon states, which in the regime of strong hybridization become composites of a phonon and two triplons. We then identify the mechanism and optimal phonon frequencies by which to control a global nonequilibrium renormalization of the lattice-driven spin excitation spectrum and demonstrate that this effect should be observable in ultrafast THz experiments on a number of known quantum magnetic materials.

DOI: [10.1103/PhysRevB.107.174415](https://doi.org/10.1103/PhysRevB.107.174415)**I. INTRODUCTION**

Rapid advances in laser technology [1] have made it possible not only to probe but also to pump quantum materials in a controlled manner on ultrafast timescales and at all the frequencies relevant to excitations in condensed matter [2–4]. This has led to phenomena ranging from Floquet engineering of electronic band structures [5] to enhanced superconductivity [6] and switching of the metal-insulator transition [7]. A wide range of experimental and theoretical efforts is now under way to extend such ultrafast control to every aspect of strongly correlated materials beyond the charge, including lattice, orbital, spin, nematic, and chiral degrees of freedom [8].

Among these, spin systems offer perhaps the ultimate quantum many-body states due to their intrinsically high entanglement and relatively low-energy scales, which lead to rather clean experimental realizations. Ultrafast switching, modulation, transport, and destruction of semiclassical ordered magnetism have been achieved using light of different frequencies [9–11]. However, a direct coupling to a magnetic order parameter is often not appropriate for the dynamical control of quantum magnetic materials, and increasing attention is focused on using the lattice as an intermediary [12–16]. While “nonlinear phononics” [17–19] exploits the anharmonic lattice potential, to date for low-frequency magnetic control [20], “magnetophononics” [21] uses harmonic phonons to effect the highly nonlinear modulation of exchange-type interactions [22].

The magnetophononic mechanism is ideally suited to the task at hand, namely studying how driving by coherent light can influence the magnetic properties of an insulating low-dimensional quantum spin system. Unless the magnetic interactions are highly anisotropic, the direct coupling of electromagnetic waves to spins is very weak. Using the lattice to mediate this coupling means choosing an infrared (IR) phonon to excite by THz laser radiation so that a coherent lattice oscillation is triggered. Intense irradiation results in a phonon occupation sufficiently high that the (super)exchange couplings between the localized spins undergo a significant alteration [15,22,23], leading to readily detectable changes in the properties of the magnetic subsystem. While the THz laser can be used to select any IR-active phonon in the spectrum of available lattice excitations, this phonon introduces a frequency that *a priori* has no direct connection to the intrinsic excitation frequencies of the spin system. Driving a very fast phonon mode (ω_0) would put the spin system in the true Floquet regime, where one might seek spin-excitation bands shifted by $\pm n\omega_0$ (for small integer n). Finding a very slow phonon mode would allow the spin correlations and excitations to be modulated over the course of a single phonon period. Between these two limits, strong excitation of the collective spin modes at their intrinsic frequencies would go beyond these modifications of the existing magnetic states by opening the possibility of creating fundamentally different types of composite collective state, including hybrid spin-spin and spin-phonon composites.

Here we analyze the physics of the magnetophononic mechanism at strong spin-phonon coupling by considering the nonequilibrium steady states (NESS) of a minimal model consisting of an alternating quantum spin chain coupled to a bulk

*mohsen.yarmohammadi@utdallas.edu

optical phonon mode. When the phonon frequency matches the spectrum of magnetic excitations, we find strong feedback effects between the spin and lattice sectors that produce a number of unconventional phenomena. We demonstrate an intrinsic self-blocking effect, by which a driven phonon in resonance with the peak density of magnetic excitations absorbs little of the driving laser power. We compute the mutual renormalization of the lattice and spin excitations to show how the self-blocking arises from the level repulsion between the driven phonon and a macroscopic number of triplon pairs. This hybridization also induces distinctive composite phonon-bitriplon excitations that emerge for phonon frequencies near the spin-band edges. We then demonstrate how all possible phonon frequencies that lie within the spin excitation band can act with varying efficiency to cause a driving-induced global reshaping of the spin spectrum. We discuss the consequences of self-blocking and dynamical spectral renormalization for pump-probe experiments on some quantum magnetic materials known to have strong spin-phonon coupling.

The framework for our study is one we have discussed in detail in Ref. [24], where we set out to establish and analyze the equation-of-motion approach to a magnetophononically driven system. In this paper we introduced the dimerized chain as a generic model for a gapped quantum spin system, a bulk optical phonon as the most straightforward implementation of the driving mechanism, and the remainder of the phonon spectrum as the dissipative bath. We applied the Lindblad formulation [25] to derive the quantum master equations [26] and used these to perform a detailed study of the NESS of the coupled system in the regime where a weak spin-phonon coupling restricted its response largely to linear orders. This analysis revealed the ingredients and parameters of the minimal magnetophononic model, characterized both phonon and spin NESS by their frequency-dependence and wave-vector content, computed the energy flow throughout the driven and dissipative system, related this to the system temperature, and identified the onset of nonlinear feedback effects.

The present study extends the weak-coupling analysis in three key directions. The first is to strong spin-phonon coupling, to identify and investigate the phenomenology of the driven system when the mutual feedback between the spin and lattice sectors becomes strong. Because one fundamental consequence of strong coupling is strong shifts in the characteristic mode energies, the second direction is to perform systematic scans of the driving frequency. Here we comment that the reality of current experiment is somewhat removed from the NESS protocol, using ultrashort and ultra-intense pulses that both contain a broad range of frequencies and produce high-order response processes; as a result, both of these directions constitute essential steps towards an accurate description of experiment. The third direction is that, if the strong drive is used to establish a NESS whose properties differ significantly from those of the equilibrium system, an independent “probe” laser is required to read these properties, preferably by a range of methods sensitive to the magnetic as well as to the lattice sector, and we introduce such a probe.

Our considerations are directly relevant to at least two quantum magnetic materials, CuGeO_3 and $(\text{VO})_2\text{P}_2\text{O}_7$, which were found over 20 years ago to be quasi-one-dimensional alternating spin chains with extremely strong spin-phonon

coupling. In CuGeO_3 , this coupling is strong enough to drive a spin-Peierls transition into the dimerized phase below $T_{\text{sp}} = 14$ K [27], whereas $(\text{VO})_2\text{P}_2\text{O}_7$ is intrinsically dimerized and was found by raising the temperature to show strong renormalization of the phonons by the spin sector [28]. While the spectra of spin and lattice excitations were studied in detail in both materials [28–36], they have yet to be considered from the standpoint of matching drivable (IR) phonons to particular frequency regimes within their spin spectra.

The structure of this article is as follows. In Sec. II we introduce the two phonon-coupled alternating spin-chain models we study and the equation-of-motion method by which we compute their driven dynamics. In Sec. III we analyze the phenomenon of self-blocking and its origin in level repulsion. The properties of the composite phonon-bitriplon states are presented in Sec. IV for different degrees of hybridization. Section V studies the dynamical modifications of the spin excitation band and thus demonstrates the potential for spin-band engineering in quantum magnetic materials. The relevance of these findings to two very strongly spin-phonon-coupled quantum spin-chain systems, CuGeO_3 and $(\text{VO})_2\text{P}_2\text{O}_7$, is discussed in Sec. VI and Sec. VII contains a brief summary and conclusions.

II. MODELS AND METHODS

Following the logic of Ref. [24], we consider a model for a magnetophononically driven quantum spin system that is minimally complex but nevertheless contains all of the components essential for capturing the physics of real materials. We do not focus on long-ranged magnetic order, because this is not generally stable in a truly low-dimensional magnet. Thus we consider an alternating spin chain, i.e., a one-dimensional quantum magnet with gapped spin excitations. Without loss of generality, and in order to make progress with a straightforward perturbative treatment of the spin system, we use a chain with a substantial dimerization, setting the interaction on the weaker bonds (J') to half the size of the stronger bonds (J). The IR phonon acting as the intermediary between the driving laser and the spin system can couple to the magnetic interactions in a wide variety of different ways. Here we restrict our considerations to the leading (linear) term in a Taylor expansion and analyze the two distinct coupling geometries shown in Fig. 1, where (i) the phonon modulates the strong (intradimer) bond [Fig. 1(a)], to which we refer henceforth as the “ J -model,” and (ii) the phonon modulates the weak (interdimer) bond [Fig. 1(b)], which we call the “ J' -model” [37]. We will show that the two models yield very similar results for certain magnetophononic phenomena but are quite different for other phenomena.

A. Hamiltonian dynamics

The Hamiltonian of the spin system takes the form

$$H_s = \sum_{i=1}^N (J\vec{S}_{1,i} \cdot \vec{S}_{2,i} + \lambda J\vec{S}_{2,i} \cdot \vec{S}_{1,i+1}), \quad (1)$$

where $\lambda = J'/J$, i labels the dimer, 1 and 2 denote the two spins within each dimer, and periodic boundary conditions are

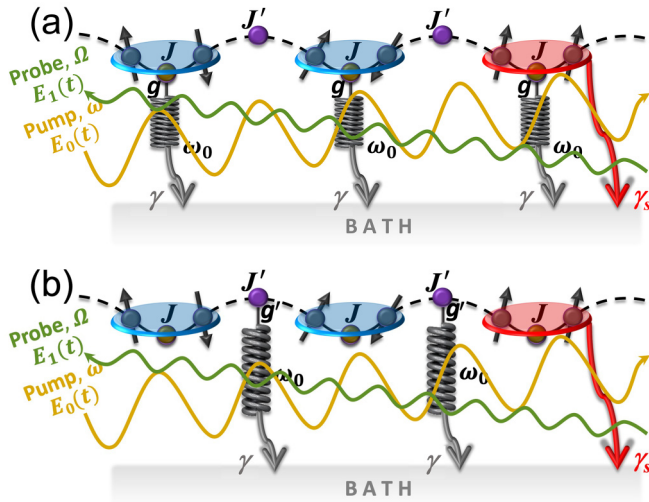


FIG. 1. Magnetophononically driven alternating spin chain. (a) Schematic representation of a spin chain with interaction parameters J and J' , spin damping γ_s , and spin-phonon coupling g to the strong bond (J); we refer to this system as the J -model. (b) Analogous model with spin-phonon coupling g' only to the weak bond (J') of the alternating spin chain, to which we refer as the J' -model. In both panels, blue (darker) ellipses denote dimer singlets and the red (lighter) ellipse a triplon excitation. The phonon frequency is ω_0 and its damping is γ , the pump laser drives the system at any frequency, ω , with electric field E_0 , and a weaker probe beam addresses it at frequency Ω with field $E_1 \ll E_0$.

assumed. The full phonon Hamiltonian is

$$H_{p,BZ} = \sum_{q \in \text{BZ}} \omega_{\text{ph}}(q) b_q^\dagger b_q, \quad (2)$$

where we have omitted an additional quantum number for the different phonon branches. The acoustic phonons make the largest contributions to the damping, both of optical phonons and of spin excitations, and as a result their effects are included in the phenomenological damping coefficients to be introduced below. For the purposes of magnetophononic driving, we use the frequency of the incoming THz laser radiation to select a single, IR-active optical phonon, which without loss of generality can be dispersionless. The only relevant phonon momentum is $q = 0$, because of the dispersion relation (extremely high speed) of the incident light, and hence any phonon dispersion plays no role. The only phonon term in the Hamiltonian of the driven system is then

$$H_p = \omega_0 b_0^\dagger b_0, \quad (3)$$

where we use b_0 and ω_0 as shorthand for $b_{q=0}$ and $\omega_{\text{ph}}(q = 0)$. A further Hamiltonian term is required to describe the driving of this phonon by the electric field $E_0(t)$ of the laser,

$$H_1 = \sum_{i=1}^N E_0(t) (b_i^\dagger + b_i) = N E_0(t) \hat{d}, \quad (4)$$

where $\hat{d} = (b_0^\dagger + b_0)/\sqrt{N}$ is the operator specifying the local atomic displacement. The linear dependence on N indicates clearly that any finite driving induces a finite

value of the phonon displacement observable, $q(t) = \langle \hat{d} \rangle$, and hence a macroscopic occupation ($n_0 \propto N$) of the $q = 0$ boson.

To complete the magnetophononic Hamiltonian we specify the two types of spin-phonon coupling shown in Fig. 1. For the J -model,

$$H_{\text{sp},J} = \sum_{i=1}^N g (b_i + b_i^\dagger) [\vec{S}_{1,i} \cdot \vec{S}_{2,i} - \langle \vec{S}_{1,i} \cdot \vec{S}_{2,i} \rangle_{\text{eq}}], \quad (5)$$

where the second term denotes the equilibrium value of the spin interaction on the strong bonds of the chain, and its presence ensures that the dimerization λ does not change in absence of the driving term. For the J' -model,

$$H_{\text{sp},J'} = \sum_{i=1}^N g' (b_i + b_i^\dagger) [\vec{S}_{2,i} \cdot \vec{S}_{1,i+1} - \langle \vec{S}_{2,i} \cdot \vec{S}_{1,i+1} \rangle_{\text{eq}}]. \quad (6)$$

The spin-phonon coupling coefficients have units of energy, and for convenience we will normalize g to J and g' to J' . While the two coupling types are dichotomous, in almost any real material one may expect the atomic displacements associated with any phonon mode to include components that alter all of the magnetic interaction terms in the system.

We proceed by diagonalizing the spin system, for which we introduce bond operators expressing the creation and annihilation of singlet and triplet states on each dimer i . In the relevant limit, where small numbers of triplets form the elementary excitations (henceforth ‘‘triplons’’) above a sea of singlets, the exact identity [38,39]

$$S_{1(2),i}^\alpha = \frac{1}{2} [\pm (s_i^\dagger t_{\alpha,i} + t_{\alpha,i}^\dagger s_i) - i \epsilon_{\alpha\beta\gamma} t_{\beta,i}^\dagger t_{\gamma,i}], \quad (7)$$

can be reduced to

$$S_{1(2),i}^\alpha = \pm \frac{1}{2} (t_{\alpha,i} + t_{\alpha,i}^\dagger) + \mathcal{O}(t^\dagger t), \quad (8)$$

where $\alpha \in \{x, y, z\}$ denotes both the spin component and the triplon flavor. The full expression [Eq. (7)] shows explicitly how triplon creation is accompanied by singlet annihilation, and vice versa, ensuring the hard-core property of the triplons. It is also the basis of a systematic perturbative approach that could be used to perform accurate calculations for alternating chains with much weaker dimerization ($\lambda \rightarrow 1$) [40,41]. However, for the moderate values of λ that we consider ($\lambda \lesssim 1/2$), a reliable description of the elementary magnetic excitations is obtained by using only the first term of Eq. (8) (i.e., restricting the Hamiltonian to bilinear terms) and neglecting the hard-core property of the triplons [24]. A Fourier transformation and a Bogoliubov transformation, the latter using the basis of diagonal triplons $\tilde{t}_{\alpha,k}$ [24], brings the spin Hamiltonian to the form

$$H_s = \sum_{k,\alpha} \omega_k \tilde{t}_{\alpha,k}^\dagger \tilde{t}_{\alpha,k} \quad (9)$$

with dispersion relation

$$\omega_k = J \sqrt{1 - \lambda \cos k}. \quad (10)$$

To apply these transformations to the Hamiltonian describing the spin-phonon coupling, we introduce the wave-vector-dependent coefficients

$$y_k = J[1 - \lambda \cos k/2]/\omega_k, \quad (11a)$$

$$y'_k = J' \cos k/(2\omega_k). \quad (11b)$$

With these we express the J -model in the form

$$H_{\text{sp},J} = g\hat{d} \sum_{k,\alpha} \left[y_k \tilde{t}_{\alpha,k}^\dagger \tilde{t}_{\alpha,k} + \frac{1}{2} y'_k (\tilde{t}_{\alpha,k}^\dagger \tilde{t}_{\alpha,-k}^\dagger + \text{H.c.}) \right] \quad (12)$$

and for the J' -model we obtain

$$H_{\text{sp},J'} = -\frac{g'\hat{d}}{2\lambda} \sum_{k,\alpha} y'_k [2\tilde{t}_{\alpha,k}^\dagger \tilde{t}_{\alpha,k} + \tilde{t}_{\alpha,k}^\dagger \tilde{t}_{\alpha,-k}^\dagger + \text{H.c.}] \quad (13)$$

These two equations allow us to observe the leading differences and similarities of the two models. The most striking difference is that the prefactor gy_k of $\tilde{t}_{\alpha,k}^\dagger \tilde{t}_{\alpha,k}$ in the J -model is changed to $-g'y'_k/\lambda$ in the J' -model, which amounts to a sizable decrease because $|y'_k| \ll y_k$ for most k values. An intriguing similarity arises in the prefactor of the pair-creation and -annihilation terms, where gy'_k is changed to $-g'y'_k/\lambda$. The sign of the prefactor matters little, because it can be changed by the unitary transformation $\tilde{t}_{\alpha,k} \rightarrow i\tilde{t}_{\alpha,k}$, and thus we anticipate that similar results are to be expected if one compares J - and J' -models with the property $g/J = g'/J'$ (i.e., $g = g'/\lambda$). We will illustrate this situation in Secs. III and IV.

The spin-phonon coupling contains trilinear bosonic terms incorporating two triplon operators and the displacement operator \hat{d} of the driving IR phonon. We treat these trilinear terms by a dynamical mean-field approach. For the “spin part” of this term, the mean-field procedure consists of replacing \hat{d} by its expectation value, $\langle \hat{d} \rangle = q(t)$, and keeping the action of the triplon operators. For the “phonon part” of this term, we replace the spin part by its expectation value to obtain for the J -model

$$\begin{aligned} H_{\text{sp},J} &= g\hat{d} \sum_{k,\alpha} \left[y_k \langle \tilde{t}_{\alpha,k}^\dagger \tilde{t}_{\alpha,k} \rangle + \frac{1}{2} y'_k \langle \tilde{t}_{\alpha,k}^\dagger \tilde{t}_{\alpha,-k}^\dagger \rangle + \text{H.c.} \right] \\ &= gN\hat{d} (\mathcal{U}_J + \mathcal{V}_J), \end{aligned} \quad (14a)$$

where we used

$$\mathcal{U}_J = \frac{1}{N} \sum_{k,\alpha} y_k \langle \tilde{t}_{\alpha,k}^\dagger \tilde{t}_{\alpha,k} \rangle, \quad (15a)$$

$$\mathcal{V}_J = \frac{1}{N} \sum_k y'_k \text{Re} \langle \tilde{t}_{\alpha,k}^\dagger \tilde{t}_{\alpha,-k}^\dagger \rangle. \quad (15b)$$

For the J' -model we obtain the analogous form

$$H_{\text{sp},J'} = -\frac{g'\hat{d}}{2\lambda} \sum_{k,\alpha} y'_k [2\tilde{t}_{\alpha,k}^\dagger \tilde{t}_{\alpha,k} + \tilde{t}_{\alpha,k}^\dagger \tilde{t}_{\alpha,-k}^\dagger + \text{H.c.}] \quad (16a)$$

$$= -(g'/\lambda)N\hat{d} (\mathcal{U}_{J'} + \mathcal{V}_{J'}), \quad (16b)$$

where $\mathcal{V}_{J'} = \mathcal{V}_J$ and

$$\mathcal{U}_{J'} = \frac{1}{N} \sum_{k,\alpha} y'_k \langle \tilde{t}_{\alpha,k}^\dagger \tilde{t}_{\alpha,k} \rangle; \quad (17)$$

we draw attention to the replacement $y_k \rightarrow y'_k$ relative to the J -model. We stress in addition that the phonon oscillation and the expectation value of the total spin system are both extensive quantities, as a result of which their relative quantum fluctuations tend to zero in the thermodynamic limit ($N \rightarrow \infty$), which provides an excellent justification for the mean-field decoupling we employ.

B. Quantum master equations

If a real quantum mechanical system is driven continuously, the absorbed energy will cause heating, which will on some timescale push the system beyond its quantum regime, if not also to very high temperatures (with modern laser intensities one may even surpass the melting point). A systematic treatment of the energy flow requires the considerations of an open quantum system, where relaxation and dissipation channels are included in addition to the external drive. For the spin chain pumped by an IR optical phonon (Fig. 1), we showed in Ref. [24] that the dissipation should be included on two levels, specifically the damping of the driven IR phonon and a direct damping of the triplon modes. Both are assumed to have their microscopic origin in the ensemble of phonon modes, particularly the acoustic ones, and both are treated by means of the adjoint Lindblad master equation [26]

$$\begin{aligned} \frac{d}{dt} \langle O \rangle(t) &= i \langle [H, O(t)] \rangle + \frac{1}{2} \sum_j \gamma_j \langle [L_j^\dagger, O(t)] L_j \rangle \\ &\quad + L_j^\dagger \langle O(t), L_j \rangle, \end{aligned} \quad (18)$$

where H is the Hamiltonian of the isolated system (the spin sector and the driven phonon), $O(t)$ is an operator in the Heisenberg picture, $\{L_j\}$ are Lindblad operators (operators of the isolated system that link it to its environment, the “bath”), and $\{\gamma_j\}$ are the corresponding damping coefficients (decay rates). The Lindblad framework requires that the coefficients $\{\gamma_j\}$ be relatively weak, but places no constraint on the terms within the isolated system, meaning that it can be applied for all values of g and g' [Eqs. (5) and (6)].

To describe the dissipation of the phonon, we follow the conventional choice [26] $L_1 = b_0^\dagger$, $L_2 = b_0$, and parametrize the decay rates using

$$\gamma_1 = \gamma n(\omega_0), \quad \gamma_2 = \gamma [1 + n(\omega_0)], \quad (19)$$

where $n(\omega)$ is the bosonic occupation number at energy $\hbar\omega$. The dynamics of the phonon are then that of a driven and damped harmonic oscillator,

$$\frac{d}{dt} q(t) = \omega_0 p(t) - \frac{1}{2} \gamma q(t), \quad (20a)$$

$$\frac{d}{dt} p(t) = -\omega_0 q(t) - 2\tilde{E}(t) - \frac{1}{2} \gamma p(t), \quad (20b)$$

$$\frac{d}{dt} n_{\text{ph}}(t) = -\tilde{E}(t) p(t) - \gamma n_{\text{ph}}(t), \quad (20c)$$

where $p(t) = i(b_0^\dagger - b_0)/\sqrt{N}$ is the momentum conjugate to $q(t)$,

$$n_{\text{ph}}(t) = \frac{1}{N} \langle b_0^\dagger b_0 \rangle \quad (21)$$

is the number of phonons per dimer, and $\tilde{E}(t)$, which denotes the effective electric field acting on the phonon in the presence of its coupling to the spin system, is defined for the J -model by

$$\tilde{E}(t) = E_0(t) + g[\mathcal{U}_J(t) + \mathcal{V}_J(t)] \quad (22)$$

and for the J' -model by

$$\tilde{E}(t) = E_0(t) - (g'/\lambda)[\mathcal{U}_{J'}(t) + \mathcal{V}_{J'}(t)]. \quad (23)$$

To describe the dissipation of the triplons, we proceed in a similar way by choosing the Lindblad operators for each triplon k mode to be $L_1 = \tilde{t}_{\alpha,k}^\dagger$ and $L_2 = \tilde{t}_{\alpha,k}$, with the corresponding decay rates given by

$$\gamma_1 = \gamma_s n(\omega_k), \quad \gamma_2 = \gamma_s [1 + n(\omega_k)]. \quad (24)$$

Taking γ_1 and γ_2 to be independent of α is a consequence of the isotropy of the spin system, but taking them to be independent of the momentum $\hbar k$ is a simplifying approximation that we make to avoid overburdening the model with a multitude of parameters. This assumption can be justified by the fact that we consider a one-dimensional spin system whose energy is dissipated into a bath of three-dimensional phonons. In this geometry, for any given wave vector k in the chain direction there remain two perpendicular directions over which one has to sum in order to capture the full phonon bath, whence one does not expect a strong dependence on k within this continuum of dissipation channels.

Here we remind the reader that the Lindblad operators $\tilde{t}_{\alpha,k}^\dagger$ and $\tilde{t}_{\alpha,k}$ correspond to the creation and annihilation of a quasiparticle with spin. As a consequence, these assumed bath processes do not conserve the total spin and thus are not in fact consistent with the form of the spin-phonon coupling assumed in Eqs. (5) and (6), where the isotropy of the spin part means that a phononic damping process cannot change the spin quantum number. As explained in detail in Ref. [24], this inconsistency would be repaired for a spin-isotropic material by assuming a more complex and spin-conserving form for the bath operators (for example $C_{kq} = \tilde{t}_{\alpha,k}^\dagger \tilde{t}_{\alpha,q}$) and for a material with anisotropic spin interactions, usually a consequence of finite spin-orbit couplings, by adopting a more complex form for the spin-phonon coupling. However, to make progress in elucidating the phenomenology of strong-coupling magnetophononics in the most transparent way possible, we proceed with the present minimalist formulation of the problem captured by the spin-chain model of Sec. II A.

The equations of motion for the spin sector of the J -model that result from the Lindblad master equation [Eq. (18)] take the form

$$\frac{d}{dt} u_k(t) = 2gq(t)y'_k w_k(t) - \gamma_s u_k(t), \quad (25a)$$

$$\frac{d}{dt} v_k(t) = -2[\omega_k + gq(t)y_k]w_k(t) - \gamma_s v_k(t), \quad (25b)$$

$$\begin{aligned} \frac{d}{dt} w_k(t) &= 2[\omega_k + gq(t)y_k]v_k(t) - \gamma_s w_k(t) \\ &+ 2gq(t)y'_k \left[u_k(t) + \frac{3}{2} \right], \end{aligned} \quad (25c)$$

where

$$u_k(t) = \sum_{\alpha} \langle \tilde{t}_{\alpha,k}^\dagger \tilde{t}_{\alpha,k} \rangle, \quad z_k(t) = \sum_{\alpha} \langle \tilde{t}_{\alpha,k}^\dagger \tilde{t}_{\alpha,k}^\dagger \rangle, \quad (26a)$$

$$v_k(t) = \text{Re } z_k(t), \quad w_k(t) = \text{Im } z_k(t). \quad (26b)$$

Analogously, for the J' -model we obtain

$$\frac{d}{dt} u_k(t) = -2(g'/\lambda)q(t)y'_k w_k(t) - \gamma_s u_k(t), \quad (27a)$$

$$\frac{d}{dt} v_k(t) = -2[\omega_k - (g'/\lambda)q(t)y'_k]w_k(t) - \gamma_s v_k(t), \quad (27b)$$

$$\begin{aligned} \frac{d}{dt} w_k(t) &= 2[\omega_k - (g'/\lambda)q(t)y'_k]v_k(t) - \gamma_s w_k(t) \\ &- 2(g'/\lambda)q(t)y'_k \left[u_k(t) + \frac{3}{2} \right]. \end{aligned} \quad (27c)$$

The full system of equations of motion then contains three equations for the driving phonon and $3N$ for the triplons (for a system consisting of N dimers). Because every triplon k mode is coupled to the phonon variables, and the latter to sums over all the triplons, the system cannot be split into N separate sets of differential equations. The inversion symmetry of the chain ensures that $y_k = y_{-k}$, $y'_k = y'_{-k}$, $u_k = u_{-k}$, $z_k = z_{-k}$, and $\omega_k = \omega_{-k}$, which reduces the $3N$ triplon equations to $3(N+1)/2$ for odd N . We solve these coupled differential equations numerically with an adaptive Runge-Kutta solver, which allows long times t to be accessed reliably. The chain lengths we consider vary between $N = 1001$ and 4001 in order to ensure that finite-size effects are well controlled in all regimes.

In the analyses to follow, we will characterize the system by introducing a number of measures. For the spin system it is convenient to use the number of excited triplons per dimer, which is given by

$$n_x(t) = \frac{1}{N} \sum_k u_k(t). \quad (28)$$

If a system is driven at frequency ω , for a time sufficiently long that it has reached a NESS, no other frequency will appear in the expectation values of the observables, regardless of the available fundamental frequencies in the system (notably ω_0 when this differs from ω). Only higher harmonics at integer multiples of ω will appear, and these are expected in any coupled system [24]. In order to focus on the important average values of the time-dependent quantities, for any expectation value $X(t)$ we define

$$X_0 = \frac{1}{T} \int_t^{t+T} X(t) dt, \quad (29)$$

which represents the average of X over one period, $T = 2\pi/\omega$. Below we will consider quantities including $n_{\text{ph}0}$, n_{x0} , and $u_{k,0}$. Only if one considers the transients appearing directly after switching on the drive do the average values X_0 acquire a time dependence $X_0(t)$ [24].

The focus of our calculations is on the NESS of the driven, dissipative system. We consider a representative alternating chain with moderate dimerization, $\lambda = 0.5$ in Eq. (10), which places the edges of the two-triplon excitation band at $2\omega_{\text{min}} = 1.414J$ and $2\omega_{\text{max}} = 2.449J$ [24]. When the spin-phonon

coupling is weak, NESS formation requires a timescale of approximately $5/\gamma_s$, i.e., five time constants of the spin system [24]. However, at large g values one may anticipate strong feedback processes between the phonon and spin sectors, making it necessary to examine the situation in detail, and potentially to wait for significantly longer times to ensure NESS formation. An example of complementary phonon and spin NESS, each characterized by their number operators, is shown in the time domain for a nonresonant phonon frequency in Figs. 2(a) and 2(b) at weak, strong, and very strong values of g . Here we have set the driving frequency to the phonon frequency ($\omega = \omega_0$), but neither lies within the two-triplon band. It is clear that both time traces contain increasingly complex combinations of harmonics as g is increased, with second-harmonic contributions dominating at the chosen frequency, and also that the amplitude of the oscillatory part of the phonon occupation behaves nonmonotonically as a function of g , becoming suppressed at very strong g . The oscillatory part of the triplon occupation rises very strongly with g on exiting the weak-coupling regime, but is also suppressed at very strong coupling. The corresponding static parts of both occupations are considered in Sec. III below. Concerning the timescale for NESS formation, Fig. 2(c) shows how the initial rise of n_{ph} is truncated by the rise of n_x [Fig. 2(d)]. In this nonresonant regime, at $g = 0.3J$ there remains a significant time lag between the driving phonon and the following triplon occupations, where the latter limit the former and convergence requires one slow oscillation cycle, whose length is determined by the feedback process. At $g = 0.5J$, the lag in response is much shorter and several slow oscillation cycles are required.

We close our technical presentation with a number of comments. The equations of motion are valid at all times from the onset of driving ($t = 0$) to infinity and for all applied electric fields, as well as for all phonon occupations up to the Lindemann melting criterion ($n_{\text{ph}} \approx 3$). With the present simplified treatment of the spin sector, they are valid up to a triplon occupation of order $n_x \approx 0.2$, beyond which a more sophisticated numerical treatment should be used to account for the hardcore occupation constraint. Because the equations of motion are based on a mean-field decoupling of the spin and lattice sectors, the treatment we present becomes more approximate at low phonon frequencies, specifically those below $\omega_0 = 0.2-0.3J$ [24]. Nevertheless, one may verify by considering the energy flow through the strongly spin-phonon-coupled system that the mean-field approximation remains very accurate at all phonon frequencies close to resonance with the spin system.

Finally, one may question the stability of the alternating chain in the presence of phononic driving, particularly when this is very strong or very slow. In fact the sharp fall in the driven phonon occupation at very small ω_0 in Figs. 3(a) and 3(d) below is related to a ground-state instability of the chain, where a stimulated distortion can occur (the average phonon displacement, q_0 , becomes finite) in the presence of sufficiently slow phonons. One may show that the stability criterion takes the form $\omega_0^c > F(\lambda)g^2\lambda^2J$, and that for a J -model with $\lambda = 0.5$ and $g/J = 0.5$ this critical value is $\omega_0^c \simeq 0.07J$, while in a J' -model with $\lambda = 0.5$ and $g'/J' = 0.5$ it is $\omega_0^c \simeq 0.14J$.

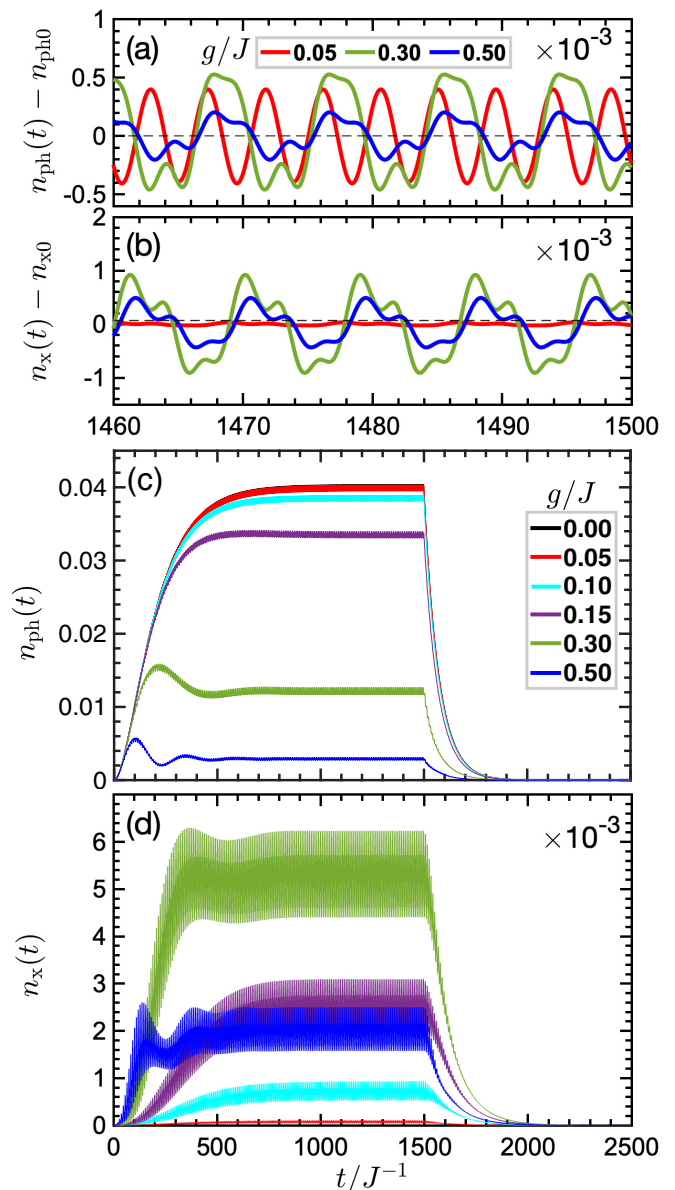


FIG. 2. Magnetophononic driving in the time domain. Examples of phonon (a) and spin NESS (b), characterized respectively by $n_{\text{ph}}(t)$ and $n_x(t)$, shown for a J -model with typical driving and damping parameters. The driving frequency is set to the phonon frequency, $\omega = \omega_0 = 0.707J$, which is set to half the lower two-triplon band-edge frequency of the isolated spin system. The development of the phonon (c) and spin responses (d) from $t = 0$ illustrates how feedback from the spin sector arrests the growth of the phonon occupation at a very early stage, although the slow, damped oscillations in the average values mean that the NESS is reached at approximately the same time in all cases. Switching off the drive at $t = 1500J^{-1}$ demonstrates that relaxation is governed entirely by the relevant damping coefficients, γ (c) and γ_s (d).

III. SELF-BLOCKING

A. NESS protocol

We consider first the NESS established by steady laser driving at the frequency of the target IR phonon, i.e., $\omega = \omega_0$. In Fig. 3(a) we show $n_{\text{ph}0}$ at this frequency choice, which we

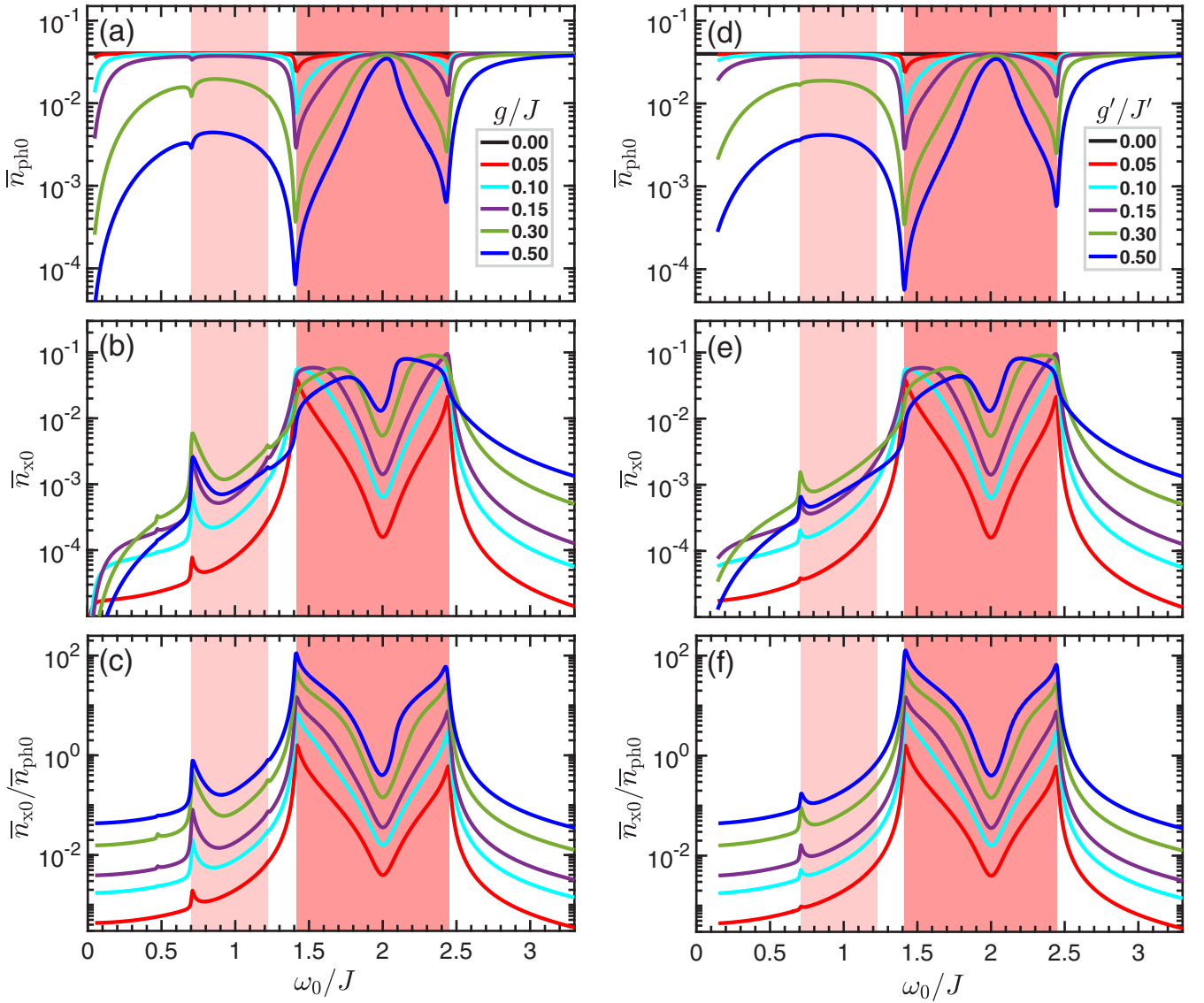


FIG. 3. Self-blocking. (a) Average driven phonon occupation, $\bar{n}_{\text{ph}0} = n_{\text{ph}0}(\omega = \omega_0)$, shown as a function of ω_0 for J -models with multiple values of g/J . The driving electric field is $E_0 = 0.2\gamma$, with $\gamma = 0.02\omega_0$ and $\gamma_s = 0.01J$. Deeper red (gray) shading marks the energy range, $2\omega_{\min} \leq \omega_0 \leq 2\omega_{\max}$, of two-tripion excitations, lighter red (gray) shading the range where two-phonon harmonic processes create these excitations. (b) Corresponding average tripton occupation $\bar{n}_{x0} = n_{x0}(\omega = \omega_0)$. (c) \bar{n}_{x0} normalized by the actual phonon occupation $\bar{n}_{\text{ph}0}$ [panel (a)]. (d) $\bar{n}_{\text{ph}0}$ shown as a function of ω_0 for J' -models with multiple values of g'/J' under the same standard driving and damping conditions. (e) Corresponding average tripton occupation \bar{n}_{x0} . (f) \bar{n}_{x0} normalized by $\bar{n}_{\text{ph}0}$ [panel (d)].

denote $\bar{n}_{\text{ph}0}$, as ω_0 is varied across the full frequency range for the J -model. We use a laser electric-field strength ($E_0 = 0.2\gamma$, expressed in energy units with $\hbar = 1$) and phonon damping ($\gamma = 0.02\omega_0$) that we maintain constant for the remainder of the analysis, and refer to these henceforth as standard driving and damping conditions. At small g , $\bar{n}_{\text{ph}0}$ is effectively constant for all ω_0 , but as g is increased we observe an increasing suppression of $\bar{n}_{\text{ph}0}$ that sets in precisely where the density of two-tripion excitations is highest, i.e., at $2\omega_{\min} = 1.414J$ and $2\omega_{\max} = 2.449J$. This resonant effect becomes gigantic at strong g , suppressing the phonon occupation by nearly three orders of magnitude at $2\omega_{\min}$.

We have named this effect “self-blocking” because the magnetic system acts to block its own energy uptake by suppressing the driven phonon. This behavior is surprising if one

expects stronger energy absorption when more spin excitations coincide with the driving laser frequency. Its explanation lies in the fact [24] that in magnetophononic driving the spin system is not coupled to the light, but only to the driven phonon. In the NESS protocol, the light frequency is fixed but the effective phonon frequency is altered by its hybridization with the spin system, which causes a level repulsion that makes the laser driving nonresonant. Spin-phonon coupling is an intrinsic property of any solid-state magnetic system and leads in materials with strong g to appreciable shifts of the spin and phonon frequencies; self-blocking in the presence of a driving term is thus an observable consequence of hybridization, but the driving does not induce the blocking. In this sense our use of terminology differs from “self-induced transparency” [42], which refers to the situation where the

external drive (the light) alters the properties of the medium in such a way that its own propagation is modified.

Analytically, self-blocking arises in the NESS protocol from the fact that the prefactor of the phonon momentum $p(t)$ in the master equation for $n_{\text{ph}}(t)$ [Eq. (20c)] is not the driving electric field $E_0(t)$, but the quantity $\tilde{E}(t)$ specified in Eqs. (22) and (23). This effective feedback from the spin system is both strongly nonlinear in g and strongly negative, acting to cancel $E_0(t)$ almost completely when ω_0 is at resonance with the band edges [Fig. 3(a)]. Despite the approximate symmetry of the two-triplon band, self-blocking is weaker by a factor of 10 at $2\omega_{\text{max}}$ due to matrix elements within the feedback process.

Turning to the response of the spin system, Fig. 3(b) shows the corresponding average triplon occupancy, \bar{n}_{x0} . The most striking feature is the strong rounding of the in-band response as g is increased. The band-edge peaks are entirely blunted by the strong suppression of $\bar{n}_{\text{ph}0}$ [Fig. 3(a)]. We stress that the effective limiting value $\bar{n}_{x0} \approx 0.1$ visible in Fig. 3(b) is purely a consequence of the giant self-blocking, and is not connected with the hard-core nature of the triplon excitations, which has not been included in the formalism of Sec. II. This rounding indicates an increasing localization of the spin response, by which the band character of the triplons becomes less relevant under strong driving by the entirely local phonon. Figure 3(b) also displays a somewhat counterintuitive nonmonotonic behavior for frequencies close to the band edges, where increasing g leads to a lower number of excited triplons due to the lower number of driving phonons caused by the self-blocking. Normalizing \bar{n}_{x0} to $\bar{n}_{\text{ph}0}$, as shown in Fig. 3(c), reveals a set of near-identical response curves sorted in ascending order of g , and hence that larger values of the spin-phonon coupling do indeed lead to larger numbers of excited triplons per excited phonon.

Still one might suspect that self-blocking is a special feature of a strongly dimerized J -model, in the sense that a $k = 0$ phonon coupled strongly to the intradimer bonds could push the system into a completely local limit of isolated spin dimers. However, to show that self-blocking is a general feature of a magnetophononic model that occurs also when the geometry does not allow the phonon to cut the spin system into local subsystems, we consider the properties of the J' -model, illustrated in Fig. 3(d). It is clear on the qualitative level that the self-blocking phenomenon is identical, with strong suppression of the absorbed laser energy, and hence of the driven phonon occupation, setting in at the band edges and rising dramatically with g' . On the quantitative level, if one compares models with the same values of g/J and g'/J' the results for $\bar{n}_{\text{ph}0}$ and \bar{n}_{x0} [Fig. 3(e)], and thus for the normalized quantity $\bar{n}_{x0}/\bar{n}_{\text{ph}0}$ [Fig. 3(f)], are similar to the degree that they cannot be distinguished on logarithmic intensity scales. This is a consequence of the close similarities between the spin-phonon coupling terms, and by extension between the equations of motion, discussed in Sec. II. We comment also that in both models the dominant self-blocking effects are concentrated around the edges of the two-triplon spectrum of the isolated spin system, indicating that, despite any tendency towards localization favored by the strong phonon coupling, the band character of the spin system is largely preserved.

Away from the two-triplon band, in Figs. 3(a) for the J -model and Fig. 3(d) for the J' -model we also observe a significant suppression of phonon energy entering the system at any frequency $\omega_0 < 2\omega_{\text{min}}$. This nonresonant self-blocking is also nonlinear in g , exceeding one order of magnitude at $g = 0.5J$ and $g' = 0.5J'$. Its appearance only in the low- ω_0 regime, but not at $\omega_0 > 2\omega_{\text{max}}$, points to an origin in multiple harmonic processes ($2\omega_{\text{min}} \leq n\omega_0 \leq 2\omega_{\text{max}}$) [24]. Although only the two-phonon harmonic ($n = 2$) at ω_{min} is visible directly, stronger g distributes the response of the system to a given $n\omega_0$ across a broader range of frequencies. By contrast, a driving phonon at the band center ($\omega_0 = 2J$) has vanishing matrix elements ($y'_{\pi/2} = 0$) with the resonant spin modes, and hence $\bar{n}_{\text{ph}0}$ recovers almost to its $g = 0$ or $g' = 0$ values for all g or g' .

To understand the context of these results, we stress again that our results are obtained for an idealized NESS experiment, where, as stated in Sec. II, in the long-time limit there are no frequencies in the system other than ω , which has been selected equal to ω_0 , and multiples thereof. In this sense the panels of Fig. 3 must be interpreted “vertically,” because there is no possibility of spectral-weight transfer between different frequencies. Although the characteristic resonant frequencies of the spin-phonon-coupled system are shifted as g is increased, and thus the system is simply off-resonance for energy uptake, in the $\omega = \omega_0$ NESS protocol there is no other option. Hence the self-blocking observed in Fig. 3 can be sought in experiments constructed to achieve a NESS, and we have found in this limit that it is a truly giant phenomenon.

B. Pulsed protocol

For a broader view, however, one does wish to understand the full response of the driven system beyond the NESS protocol. As noted above, hybridization leading to the mutual energetic repulsion of coupled levels is a ubiquitous equilibrium phenomenon in physics, which is discussed mostly in the context of hybridization between two discrete levels. Examples include the phonon-polariton [43], exciton-polariton [44], and many other types of polariton [45] (generically hybrids of a photon with dipolar matter), atom optics with many different photon frequencies [46], magnon-phonon hybridization [47], and cavity spintronics (magnon-photon hybridization) [48]. In magnetic materials where the spin-phonon coupling mechanism is more complex (less isotropic) than in Eqs. (5) and (6), the mutual repulsion (anticrossing) of phonon and one-magnon excitations can be observed in reciprocal space [49]. The key point for driving purposes is that the bare spin and phonon dispersion relations are not the characteristic resonant frequencies of the system. Before presenting our results for systems with fixed phonon frequencies ω_0 , driven at a range of different frequencies ω , we note that a conventional ultrafast experiment already introduces a spectrum of driving frequencies within the envelope of each ultrashort pulse, and hence allows automatically for the “horizontal” transfer of spectral weight (i.e., between frequencies). For this reason we use the terminology “pulsed protocol,” although in the remainder of the present work we will compare the NESS obtained in systems driven continuously at variable ω (with constant laser

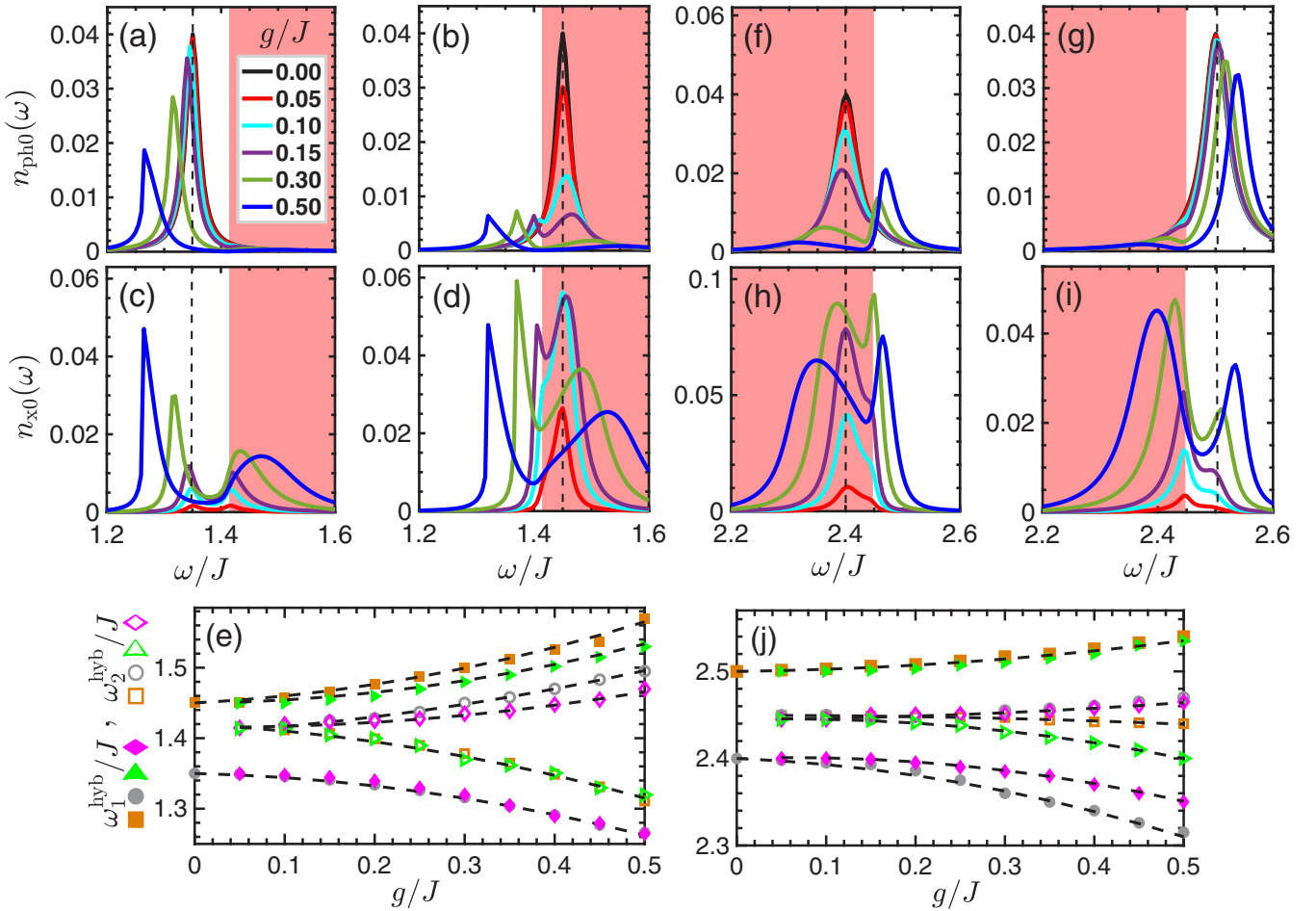


FIG. 4. Strongly hybridized excitations. (a) Phonon occupation $n_{\text{ph}0}$ shown as a function of driving frequency ω for J -models with a phonon frequency of $\omega_0 = 1.35J$ (vertical dashed line) and a range of different g values. The standard driving and damping parameters of Fig. 3 are used. (b) As in panel (a) for $\omega_0 = 1.45J$. (c) $n_{x0}(\omega)$ for $\omega_0 = 1.35J$, corresponding to panel (a). (d) $n_{x0}(\omega)$ for $\omega_0 = 1.45J$, corresponding to panel (b). (e) Peak-pair frequencies, labeled ω_1^{hyb} and ω_2^{hyb} , taken from panels (a)–(d), shown for all calculated g values; the dashed lines indicate a g^2 form. (f) $n_{\text{ph}0}(\omega)$ shown for J -models with a phonon frequency of $\omega_0 = 2.4J$ at the same set of g values and with the same standard driving and damping. (g) As in panel (f) for $\omega_0 = 2.5J$. (h) $n_{x0}(\omega)$ for $\omega_0 = 2.4J$, corresponding to panel (f). (i) $n_{x0}(\omega)$ for $\omega_0 = 2.5J$, corresponding to panel (g). (j) Peak-pair frequencies taken from panels (f)–(i); the dashed lines indicate a g^2 form.

intensity), leaving the accurate modeling of pulsed driving to a future study.

We focus primarily on the J -model and, because self-blocking is strongest at the band edges, in Fig. 4 we consider phonon frequencies, marked by the vertical dashed lines, just below and above each of the band edges. Figure 4(a) makes clear that the phononic response of a system driven at a frequency just below the lower band edge (here $\omega_0 = 1.35J$) has a conventional Lorentzian resonance centered at the bare phonon frequency for small g , but is weakened and pushed away from the band edge at stronger g . Figure 4(b) shows the analogous result when ω_0 lies just inside the spin band, where the phonon peak is damped very strongly with increasing g , and also moves away from the band edge. We stress that this is a level-repulsion effect involving all of the zero-momentum triplon-pair states, meaning a macroscopic number of levels. This situation is also evident in the fact that the hybridized phonon mode inside the band is accompanied by the development of a second feature, appearing at $2\omega_{\text{min}}$ at $g = 0.1J$, which is repelled below the band edge as g increases. The

corresponding spin response [Figs. 4(c) and 4(d)], which we analyze in Sec. IV below, makes much clearer the way in which the many triplon-pair states hybridizing with the driven phonon appear as two mutually repelling peak features in the many-body response. We note that the characteristic excitation frequencies are shifted significantly away from ω_0 and $2\omega_{\text{min}}$ at large g , and that the situation for phonon frequencies ($\omega_0 = 2.4J$ and $2.5J$) bracketing the upper band edge is exactly analogous, although with a slightly weaker mutual repulsion [Figs. 4(f)–4(i)].

In the context of self-blocking, these results show how the phononic response is shifted “horizontally,” losing its overlap with the bare response curve, as g increases. This shift is the physical reason underlying the rapid drop in the quantity $\bar{n}_{\text{ph}0}$ (i.e., for driving at $\omega = \omega_0$). Nevertheless, we stress again that driving at frequency ω produces a response only at frequencies $n\omega$, with no spectral-weight transfer to neighboring frequencies: Figure 4 was prepared by driving at every individual frequency ω represented on the x axes and by solving Eqs. (22) and (23) to obtain the NESS at each ω . Thus Fig. 4

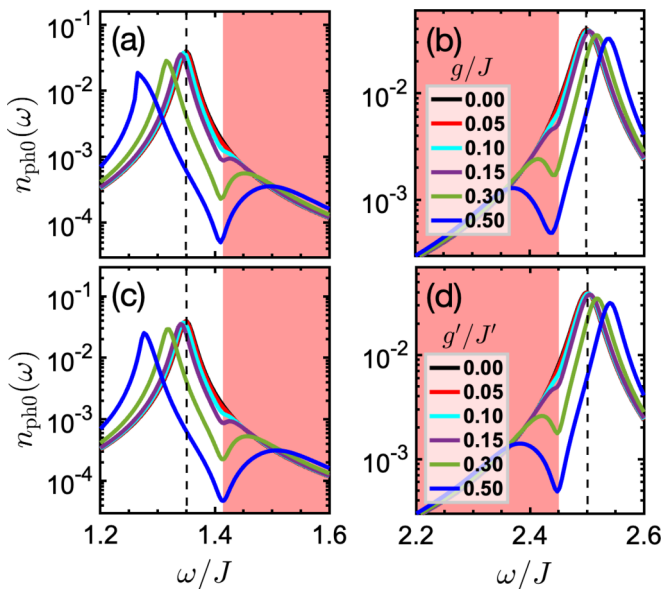


FIG. 5. Phononic response to band-edge driving. (a) Phonon occupation $n_{\text{ph}0}(\omega)$ shown on a logarithmic axis at $\omega_0 = 1.35J$ for J -models with selected values of g . The standard driving and damping parameters of Fig. 3 are used. (b) As in panel (a) at $\omega_0 = 2.5J$. [The same data are shown on a linear scale in Figs. 4(a) and 4(g).] (c) $n_{\text{ph}0}(\omega)$ shown on a logarithmic axis at $\omega_0 = 1.35J$ for J' -models with selected values of g' . (d) As in panel (c) for $\omega_0 = 2.5J$.

can be used to pose the question of whether any self-blocking is present if the laser frequency is adjusted to resonance with the peak of the phononic response at each value of g . In this situation one observes that phonons lying outside the spin excitation band undergo only a small reduction with increasing g (factors of 2 or less up to $g = 0.5J$), whereas phonons lying inside the band are suppressed by 1–2 orders of magnitude due to their hybridization with the continuum of two-triplon scattering states.

To place these results in perspective, in contrast to the conventional scenario of two-level repulsion [43–48], in the minimal magnetophononic model we find a more general form of multilevel repulsion, where a macroscopic number of zero-momentum triplon-pair states hybridize with (becoming repelled by) the driven phonon mode. This leads to a variety of features that lie beyond a two-level description, as we explore in more detail in Secs. IV and V.

IV. HYBRID PHONON-BITRIPLON STATES

As the discussion of Sec. III B made clear at the qualitative level, the hybridization of phononic and magnetic excitations is fundamental to the properties of any spin-phonon-coupled system, and thus to the phenomenology of magnetophononic driving. To elucidate the nature of the states created by the coupling of the driving phonon to the ensemble of triplon pairs, we proceed to a quantitative analysis of the frequency shifts and consider the extent of hybridization within these composite collective entities.

Returning to the features of Fig. 4, we have already remarked on the appearance of two mutually repelling excitation features when the system is driven at a phonon frequency

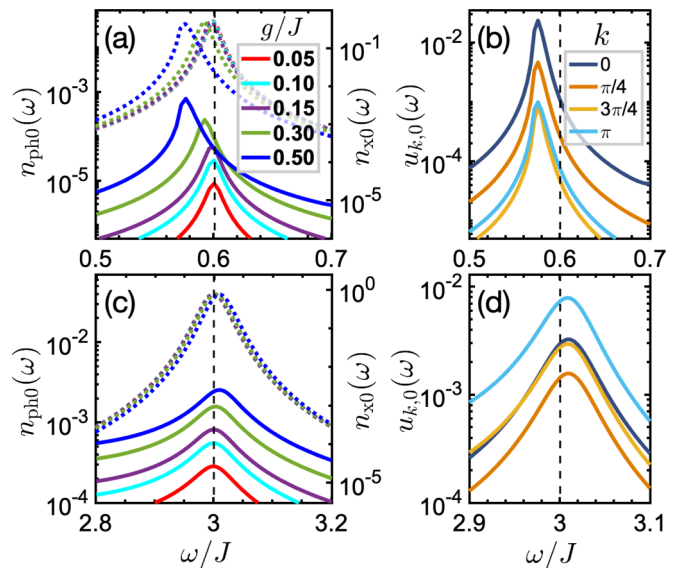


FIG. 6. Weakly hybridized excitations. (a) Phonon occupation $n_{\text{ph}0}(\omega)$ (dotted lines), and triplon occupation $n_{x0}(\omega)$ (solid lines), shown for J -models with a phonon frequency of $\omega_0 = 0.6J$ and the same set of g values as in Fig. 4. The standard driving and damping parameters of Fig. 3 are used. (b) k -resolved components of the average $u_k(\omega)$ at $\omega_0 = 0.6J$ for $g = 0.5J$. (c) $n_{\text{ph}0}(\omega)$ (dotted lines) and $n_{x0}(\omega)$ (solid lines) shown for a phonon frequency of $\omega_0 = 3.0J$. (d) k -resolved components of the average $u_k(\omega)$ at $\omega_0 = 3.0J$.

close to the band edge. Because the second set of excitations is not evident in Figs. 4(a) and 4(g), where the in-band phononic response to an out-of-band ω_0 is very weak, in Figs. 5(a) and 5(b) we show the same data on a logarithmic intensity scale, confirming the presence of a second peak that grows with g . In Figs. 5(c) and 5(d) we show the analogous data obtained for J' -models with the same range of g'/J' values. Clearly, as in Sec. III A, the physics of hybrid states in the J' -model is identical to the J -model up to minor quantitative details [that can be traced to the matrix elements of the triplon pair-creation and -annihilation terms in Eqs. (12) and (13)], and thus we do not discuss the J' -model further in this section.

A key additional observation concerning the second set of excitation features is that they appear for small g at the band-edge frequencies $2\omega_{\text{min}}$ in Figs. 4(a) to 4(d), 5(a), and 5(c) and $2\omega_{\text{max}}$ in Figs. 4(f)–4(i), 5(b), and 5(d), before being repelled further from the bare phonon frequency as g is increased. Thus one obtains a picture of “magnetic” hybrid states being induced within the spin sector by the influence of the driven “phononic” state, before stronger g values cause a strong admixture of lattice and spin character.

One way to confirm the hybrid nature of these states is to begin in the regime where weak hybridization is guaranteed. In Fig. 6(a) we show the phonon and triplon occupations obtained when the driving frequency, $\omega_0 = 0.6J$, lies far below the two-triplon band. While $n_{\text{ph}0}(\omega)$ undergoes only minor changes, indicating that this is a rather well localized phononic mode, its hybridization is clearly strong enough to shift its frequency out of the regime covered by Fig. 3(a). $n_{x0}(\omega)$ indicates that a spin response does emerge with g despite the nonresonant self-blocking, and in Fig. 6(b) we show

that the magnetic dressing of the phononic mode contains all the k components of $n_{x0}(\omega)$, i.e., the phonon undergoes a weak admixture with all $(k, -k)$ triplon pairs. In Figs. 6(c) and 6(d) we show the analogous results for a driving frequency, $\omega_0 = 3.0J$, lying well above the two-triplon band, where the hybridization effects are qualitatively similar but quantitatively are much weaker. Here we do not attempt to discern the weak effects of these off-resonant driving processes at the band edges.

Returning to the regime of strong hybridization controlled by g , driving frequencies near both band edges are shown in Fig. 4. For a complete analysis of the many-level mutual repulsion, we gather the characteristic frequencies of these phonon and spin spectra in Figs. 4(e) and 4(j), which display clearly the g^2 evolution in the shift of the peak frequencies expected of hybrid excitations. To quantify the admixture of lattice and spin character, at the lower band edge one may define a hybridization parameter $s = g/|\omega_0 - 2\omega_{\min}|$, and similarly with $2\omega_{\max}$ for the upper band edge. We note that the frequencies ω_{\min} or ω_{\max} appearing in s are indicative only, because the phonon is hybridized with all the triplon pairs in the system, but the van Hove singularities at the one-dimensional band edge mean that the response is dominated by triplon pairs at these edges. A language of “phononic” and “magnetic” hybrids is useful at $\omega_0 = 0.6J$ and $3.0J$ (Fig. 6), where $s < 1$ for all g . However, when $s \approx 10$ both hybrids are strongly magnetic and phononic, and indeed the 50:50 weight distribution evident at larger g in Figs. 4(c), 4(d), 4(h), and 4(i) suggests states that are maximally hybridized.

For the hybrids repelled outside the band, the coinciding peaks in $n_{\text{ph}0}(\omega)$ and $n_{x0}(\omega)$ identify them as a strongly triplon-dressed version of the “phononic” hybrid shown in Fig. 6. The in-band hybrids lie in a continuum of propagating triplon-pair states, and thus manifest themselves as broader peaks, whose maxima lie at slightly different energies in $n_{\text{ph}0}(\omega)$ [Figs. 4(b) and 4(f)] and in $n_{x0}(\omega)$ [Figs. 4(d) and 4(h)]. We stress that the widths of these shifted peaks reflect a finite lifetime that is determined not by the damping of the bath (γ and γ_s in Sec. II) but by the intrinsic, g -mediated decay of the phonon into the triplon-pair continuum.

For the driving and damping of our system, all of the strongly hybridized states are to a good approximation “phonon-bitriplons,” in which each phonon hybridizes with one triplon pair ($\tilde{r}_k^\dagger \tilde{r}_{-k}^\dagger$) of zero net momentum. For specificity we reserve the term “phonon-bitriplon” for the composite collective entity formed at $s \geq 1$. However, it is clear that all of the hybrid states forming in a system with a spin-phonon coupling of the form described by Eqs. (5) and (6) involve the dressing of phonons by bitriplons, and conversely. We comment that the formation of composites from a boson pair and a single boson of a different kind is not common in condensed matter physics. A more common scenario is composite formation involving a boson and a pair of fermions, for example where a photon and an exciton form a polariton [44]. Scattering processes of one boson into two different bosons are somewhat more familiar, with phonon-bimagnon processes being discussed both theoretically [50,51] and experimentally [52,53] in the optical spectra of cuprate quantum magnets. Phonon-bimagnon processes at GHz frequencies are now applied increasingly in the field of magnonics [54], while

photon-bimagnon processes are engineered in cavity spintronics [48]. Similar physics could also be realized using ultracold atoms [55], where the optical lattice blurs the distinction between photon and phonon, although we are not aware of an experiment. On a very different energy scale, in particle physics the virtual decay of the Higgs boson into pairs of W or Z bosons [56,57] is an off-shell process with intermediate s , where the level repulsion of Figs. 4(e) and 4(j) is known as a “Higgs mass renormalization.”

V. SPIN-BAND ENGINEERING

In Sec. IV we showed how the coupled phonon creates one additional hybrid state in the spectrum of the system, and that its driving can cause significant shifts of spectral weight at neighboring frequencies. However, we have not yet shown whether phononic driving can alter the entire excitation spectrum (i.e., the effective bulk properties) of the spin system. At first sight one might anticipate that such global spin-band engineering is not possible while the driven phonon is completely harmonic, and that this would require the anharmonic terms considered in nonlinear phononics. Here we show that the spin-phonon coupling of our magnetophononic model introduces an intrinsic nonlinearity, and as a result that the spin spectrum can indeed be modified strongly by a harmonically driven optical phonon.

A. First-order band engineering

The leading order of a Magnus expansion [58] for time-dependent Hamilton operators consists of the time-averaged Hamiltonian. If one considers the J -model, Eqs. (25b) and (25c) describe oscillations of v_k and w_k at an average frequency $\omega_k + gq_0 y_k$ that differs for each wave vector (neglecting higher-order corrections in g), and hence the average value of v_k vanishes. Averaging Eq. (20b) implies that

$$0 = -\omega_0 q_0 - 2\tilde{E}_0, \quad (30)$$

and hence that

$$q_0 = -2g\mathcal{U}_{J0}/\omega_0 \quad (31)$$

in the J -model, meaning that the driving causes the equilibrium (stationary) position of the phonon to be displaced by a finite amount q_0 . By similar considerations for the J' -model we obtain

$$q'_0 = 2g'\mathcal{U}_{J'0}/(\lambda\omega_0). \quad (32)$$

In Fig. 7(a) we compute q_0 in the J -model, using a laser frequency resonant with the driving phonon ($\omega = \omega_0$, for which we use the notation \bar{q}_0), and in Fig. 7(b) we show our results for \bar{q}'_0 in the J' -model.

In contrast to the results of Secs. III and IV, the stationary displacements differ dramatically between the two models. The values of \bar{q}_0 are always negative and reach 4% of the lattice dimension at their maximum extent, which is one order of magnitude larger than the values of \bar{q}'_0 . The phonon frequencies most effective in controlling \bar{q}_0 are neither those at the band edges, where giant self-blocking suppresses the displacement almost completely, nor those at the band center, where the driving terms decouple, but the “quarter-band” ones

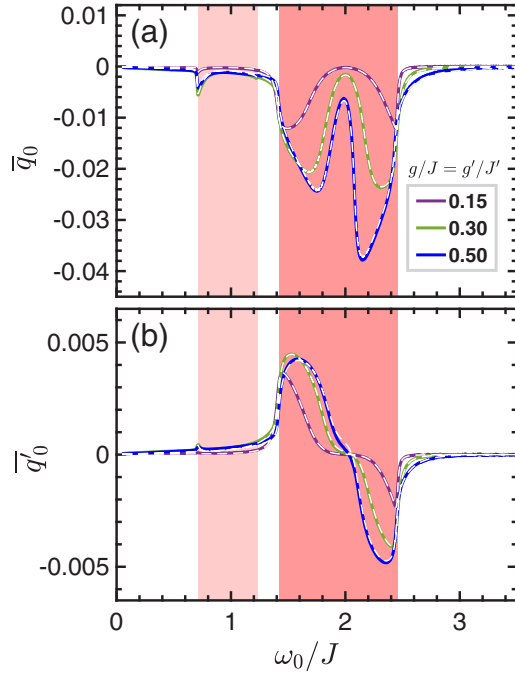


FIG. 7. Driven stationary phonon displacement. (a) Average phonon displacement \bar{q}_0 (solid lines) shown as a function of the phonon frequency for J -models with three different g values and with standard driving and damping. (b) \bar{q}'_0 (solid lines) shown as a function of the phonon frequency for J' -models with three different g' values. Note the different y-axis scales on the two panels. The dashed white lines show the quantities computed on the right-hand sides of Eqs. (31) and (32).

around $k = \pi/4$ and $3\pi/4$. A broader range of mid-band frequencies is effective in modulating \bar{q}'_0 , where the essential qualitative feature is a change in the sign of the displacement as the driving frequency is moved through the band center. The origin of these differences can be found by a closer inspection of the differential equations. In \mathcal{U}_J the matrix element is y_k , while in $\mathcal{U}_{J'}$ it is y'_k , which changes sign at $k = \pi/2$. The evolution of both quantities, shown by the dashed white lines in Fig. 7, indicates that their dominant contributions result from the resonant wave vector, k_{res} , selected by the driving phonon according to $\omega_0 = 2\omega_{k_{\text{res}}}$. The excellent agreement between the two sets of curves in Fig. 7 illustrates clearly the validity of Eqs. (31) and (32).

These stationary phonon displacements have a direct effect on the spin bands by modifying the magnetic interactions. Here we consider only the linear-order terms, which in the J -model cause the change $J \rightarrow \tilde{J} = J(1 + gq_0)$, and hence renormalize the triplon dispersion [Eq. (10)] to

$$\tilde{\omega}_k = J(1 + gq_0)\sqrt{1 - \lambda \cos k/(1 + gq_0)} \quad (33)$$

while in the J' -model $J' \rightarrow \tilde{J}' = J'(1 + g'q_0)$ yields the renormalized dispersion

$$\tilde{\omega}_k = J'\sqrt{1 - \lambda(1 + g'q_0) \cos k}. \quad (34)$$

At this linear level, the triplons retain a cosinusoidal dispersion and the band-engineering effects of the phonon separate cleanly. A phonon mode coupling strictly to the intradimer

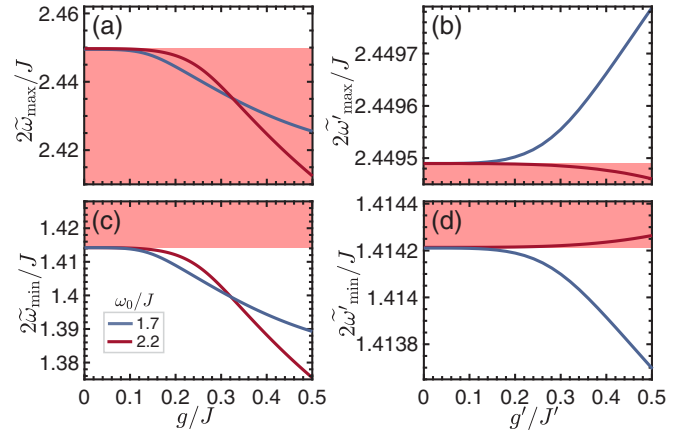


FIG. 8. Spin-band engineering. Renormalized upper [(a),(b)] and lower [(c),(d)] edges of the two-triplon excitation band of the J -model [(a),(c)] and the J' -model [(b),(d)], shown as functions of the spin-phonon coupling g for standard driving by phonons of frequencies $\omega_0 = 1.7J$ and $2.2J$. Note the differing frequency ranges relevant for the two models.

bond of an alternating spin chain will renormalize the band center downwards without changing the band width, and a phonon mode coupling strictly to the interdimer bond will renormalize the band width, upwards or downwards, without changing the band center.

With a view to later detection (Sec. V C), we define the lower and upper edges of the renormalized bands as

$$\tilde{\omega}_{\min} = \tilde{\omega}_{k=0}, \quad (35a)$$

$$\tilde{\omega}_{\max} = \tilde{\omega}_{k=\pi}, \quad (35b)$$

and in Fig. 8 we show the evolution of the two-triplon band extrema with g and g' for two phonon frequencies chosen near the lower and upper maxima of $|\bar{q}_0|$ [Fig. 7(a)]. Qualitatively, in the J -model we observe the downwards renormalization of the band center by both phonons contrasting with a weak band narrowing (for $\omega_0 = 2.2J$) or band broadening (for $\omega_0 = 1.7J$) in the J' -model. Quantitatively, the $\omega_0 = 2.2J$ phonon is more effective in the J -model and the $\omega_0 = 1.7J$ phonon in the J' -model, but far the most important observation is that our standard driving leads to percent effects on the band center [J -model, Figs. 8(a) and 8(c)] but only hundredths of a percent on the band width [J' -model, Figs. 8(b) and 8(d)].

In Fig. 9 we investigate the scope for increasing band-engineering effects by increasing the laser electric field (mindful of the increased thermal management this mandates). For the chosen value of g and g' , we find that the two-triplon band extrema display a quadratic evolution only as far as our standard driving value, $E_0 = 0.2\gamma$, before entering an extended regime of largely linear dependence. Only the band center for driving by a phonon with $\omega_0 = 1.7J$ displays a more complex behavior, due presumably to extreme feedback effects setting in at very strong fields. We remark that such strong fields, used as ultrashort pulses to control the system temperature, can yield 10% effects on the engineered band center and 1% effects on the band width.

We conclude our survey of linear-order spin-band engineering by examining its dependence on the spin damping

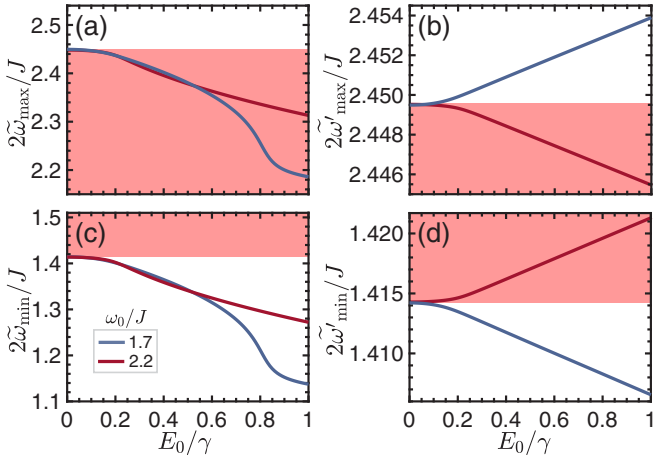


FIG. 9. Spin-band engineering by laser intensity. Renormalized upper [(a),(b)] and lower [(c),(d)] edges of the two-triplon excitation band of a J -model with $g/J = 0.3$ [(a),(c)] and a J' -model with $g'/J' = 0.3$ [(b),(d)], shown as functions of the driving laser electric field E_0 for driving by phonons of frequencies $\omega_0 = 1.7J$ and $2.2J$ and with standard damping. For reference, the standard driving field shown in all other figures is $E_0 = 0.2\gamma$.

coefficient γ_s . To do this, in Fig. 10 we show not the band extrema but the stationary phonon displacements \bar{q}_0 and \bar{q}'_0 . While the qualitative behavior of the driven stationary displacement is not changed by γ_s , it is clear that the quantitative extent follows an approximate $1/\gamma_s$ trend, and hence that the observation of spin-band engineering will require systems in which the intrinsic damping of the spin modes is weak. This result also underlines the fact that the finite driven values of \bar{q}_0 and \bar{q}'_0 result from nonlinearities introduced by the coupling to the spin system.

B. Second-order band engineering

For completeness we analyze the second-order term in the Magnus expansion. While every order of the expansion can be computed systematically [58], the convergence is rapid in the parameter regime of our present considerations and a full understanding of our calculated results can be obtained from the first- and second-order terms only. We consider the minimal Hamiltonian

$$H^{(k)} = \omega_k(t_+^\dagger t_+ + t_-^\dagger t_-) + \mu(t)(t_+^\dagger t_-^\dagger + t_+ t_-), \quad (36)$$

where t_+ creates a triplon of flavor α at $k \neq 0$ and t_- a triplon of flavor α at $-k$. The oscillating amplitude of the cross-term is $\mu(t) = g'_k q(t)$ in the J -model and $\mu(t) = -gy'_k q(t)/\lambda$ in the J' -model; we assume that $\mu(t) = \mu_0 \cos(\omega t)$ for a suitably chosen time offset, which in view of the dominant cosinusoidal behavior of $q(t)$ [24] is well justified. In the interaction picture, the dynamics of the diagonal terms is contained in the operators and the time-dependent Hamiltonian takes the form

$$H_1^{(k)} = \mu(t)(e^{2i\omega_k t} t_+^\dagger t_-^\dagger + e^{-2i\omega_k t} t_+ t_-). \quad (37)$$

The time-averaged action can be computed by the Magnus expansion as an asymptotic series in μ_0 , where as in Sec. VA the first order is given by the time average over one period ($T = 2\pi/\omega$). However, away from resonance, meaning

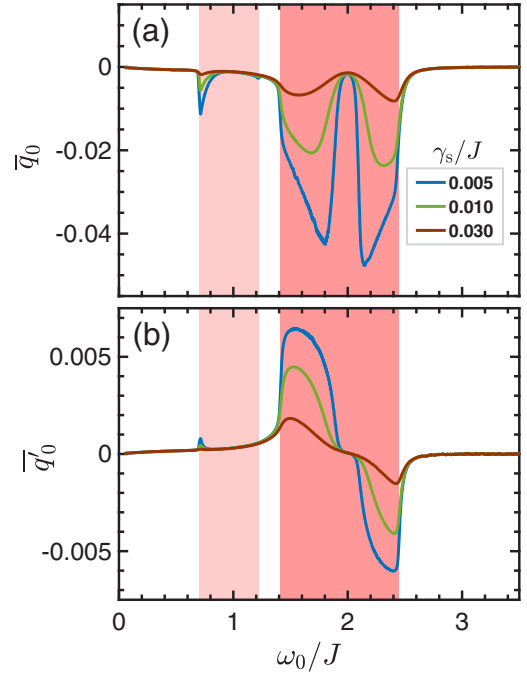


FIG. 10. Stationary phonon displacement and spin damping. (a) Average phonon displacement \bar{q}_0 shown as a function of the phonon frequency for J -models with $g = 0.3J$ and with standard driving and phonon damping, but with three different values of the spin damping, γ_s . (b) \bar{q}'_0 shown as a function of the phonon frequency for J' -models with $g' = 0.3J'$ for three different values of γ_s .

that the system is not driven near $\omega = 2\omega_k$, there is no first-order term, and this situation arises if one considers the changes to the band edges ($\omega_k = \omega_{\min}$ or $\omega_k = \omega_{\max}$) caused by driving the system with a phonon whose frequency lies well inside or outside the band.

The general form of the second-order term is

$$H_{M,2} = \frac{-i}{2t} \int_0^t dt_1 \int_0^{t_1} dt_2 [H(t_1), H(t_2)]. \quad (38)$$

Here we insert

$$\begin{aligned} & [H_1^{(k)}(t_1), H_1^{(k)}(t_2)] \\ &= \mu_0^2 \cos(\omega t_1) \cos(\omega t_2) e^{2i\omega_k(t_1-t_2)} [t_+^\dagger t_-^\dagger, t_+ t_-] - \text{H.c.}, \end{aligned} \quad (39)$$

and perform the inner integration over $t_2 \in [0, t_1]$ to obtain

$$\begin{aligned} & \int_0^{t_1} [H_1^{(k)}(t_1), H_1^{(k)}(t_2)] dt_2 \\ &= \frac{4i\omega_k \mu_0^2 \cos(\omega t_1) [\cos(2\omega_k t_1) - \cos(\omega t_1)]}{4\omega_k^2 - \omega^2} \hat{B}, \end{aligned} \quad (40)$$

where \hat{B} denotes $[t_+ t_-, t_+^\dagger t_-^\dagger] = t_+^\dagger t_+ + t_-^\dagger t_- + 1$. The t_1 integration [Eq. (38)] effects a time average in which only the $\cos^2(\omega t_1)$ term contributes $1/2$, whereas all the other combinations vanish, and thus we derive the second-order correction

$$H_{M,2} = \frac{\omega_k \mu_0^2}{\omega^2 - 4\omega_k^2} \hat{B}. \quad (41)$$

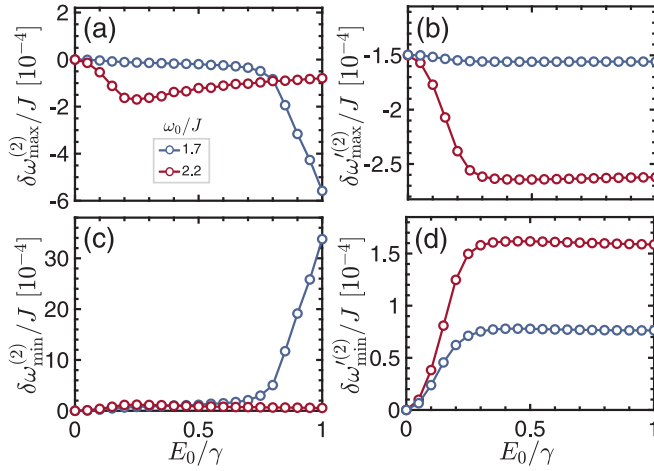


FIG. 11. Second-order correction. Frequency shift of the upper [(a),(b)] and lower [(c),(d)] edges of the two-triplon excitation band obtained at second order for a J -model with $g/J = 0.3$ [(a),(c)] and a J' -model with $g'/J' = 0.3$ [(b),(d)], shown as functions of the driving laser electric field E_0 for driving by phonons of frequencies $\omega_0 = 1.7J$ and $2.2J$ and with standard damping.

The corresponding energy shift of the two-triplon excitation band is

$$\delta\omega_k^{(2)} = \frac{\omega_k \mu_0^2}{\omega^2 - 4\omega_k^2}, \quad (42)$$

which by continuity will extend also to the band edges at $k = 0$ and $k = \pi$.

For driving in resonance with an in-band phonon, $2\omega_{\min} < \omega = \omega_0 < 2\omega_{\max}$, we deduce from Eq. (42) that $\delta\omega_{\min}^{(2)}$ is positive whereas $\delta\omega_{\max}^{(2)}$ is negative, and thus that the second-order contribution is a band narrowing. In Fig. 11 we show this correction as function of the driving laser electric field at a fixed value of $g = 0.3 = g'$. The highly nonlinear, and even nonmonotonic, behavior is a consequence of the fact that the oscillation amplitude $q(t)$ is contained within the quantity μ_0 . Nevertheless, these second-order effects are very small when compared with the first-order ones (Sec. V A), and for this reason we do not compute any higher orders. However, we will show next that the second-order corrections are indeed detectable in our calculations.

C. Detection of tailored spin bands

We turn now to the question of how to measure driving-induced spin-band renormalization in the magnetophononic protocol. Because the pump electric field, at frequency ω , is required to excite the target phonon(s) creating the desired NESS, a full characterization of the NESS properties will require the introduction of an additional frequency. Thus we introduce a further field component,

$$E(t) = E_0 \cos(\omega t) + E_1 \cos(\Omega t), \quad (43)$$

where as before E_0 is the strong pump drive and now E_1 is a significantly weaker “probe” drive, represented by the small green waves in Fig. 1. Because we are investigating NESS, both field components are continuous and the time delay used in true pump-probe studies is absent.

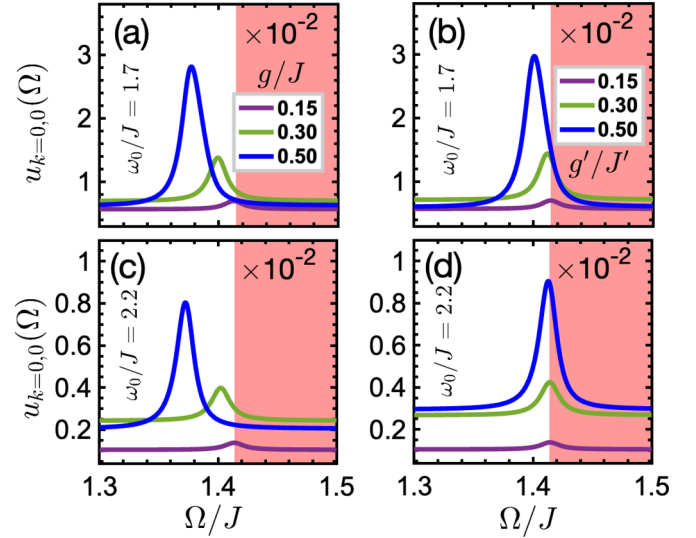


FIG. 12. Detection of spin-band engineering. Average value of $u_{k=0,0}$, shown as a function of the probe frequency Ω around the lower band edge of [(a),(c)] J -models with selected values of g/J and [(b),(d)] J' -models with selected values of g'/J' . A standard driving field, E_0 , is applied at $\omega = \omega_0 = 1.7J$ in panels (a) and (b) and at $2.2J$ in panels (c) and (d). The probe field is set to $E_1 = 0.2E_0$ and standard damping is used.

In the remainder of this subsection we consider a single driving phonon whose frequency is located within the two-triplon band ($2\omega_{\min} < \omega_0 < 2\omega_{\max}$) and pump it resonantly ($\omega = \omega_0$), while scanning the detection frequency Ω around the lower and upper band edges where the driving-induced changes are expected to be clearest. As the most sensitive diagnostic of the edges of the modified two-triplon band, we take the liberty of showing not $n_{x0}(\omega_0, \Omega)$ but the respective components $u_{k=0,0}$ to characterize the lower band edge and $u_{k=\pi,0}$ for the upper. These quantities are readily computed from the equations of motion of Sec. II and we comment below on current experimental developments in the use of coherent light as a direct probe of magnetic phenomena.

Figure 12 shows the value of $u_{k=0,0}$ measured on scanning Ω through the lower band edge for different values of the spin-phonon coupling in both the J - and the J' -model. In contrast to Figs. 4(c), 4(d), 4(h), and 4(i), which showed two band-edge peaks in $n_{x0}(\omega)$ when changing the driving frequency in the presence of a near-resonant phonon mode, here the system is driven at $\omega = \omega_0 = 1.7J$ and $2.2J$, $s < 1$, and we observe a single band-edge peak in the magnetic response. The shift of this peak away from the equilibrium band edge (shown by the red shading) increases strongly with g in the J -model [Figs. 12(a) and 12(c)], where in accordance with Fig. 8 it is downward for both phonons (and, given their relative separation from the lower band edge, surprisingly similar in magnitude). By contrast, the shift increases only weakly with g' in the J' -model, to the extent that its expected change of sign is not discernible between Figs. 12(b) and 12(d) because the shift is so weak in the latter case.

For a fully quantitative interpretation of the probe spectrum, we proceed to perform a systematic variation of all relevant parameters. In Fig. 13 we vary the pump and probe

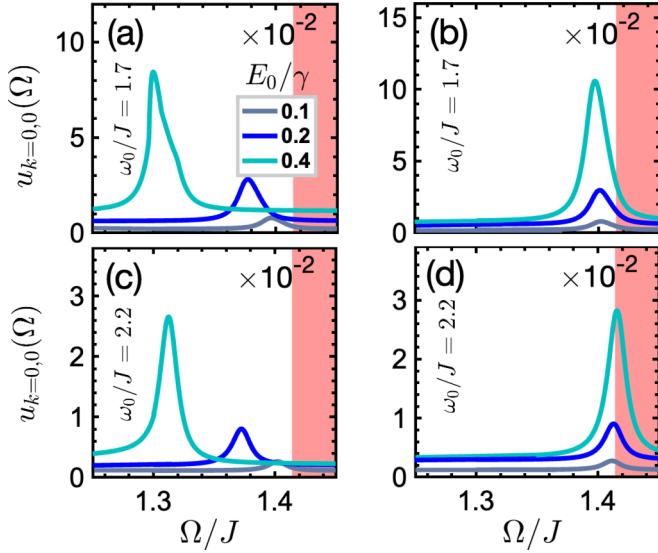


FIG. 13. Dependence of pump-probe protocol on pump amplitude. Average value of $u_{k=0}$, shown as a function of the probe frequency Ω around the lower band edge of [(a),(c)] a J -model and [(b),(d)] a J' -model with $g/J = 0.5 = g'/J'$ for different pump amplitudes, E_0 . The pump field is applied at $\omega = \omega_0 = 1.7J$ in panels (a) and (b) and at $2.2J$ in panels (c) and (d). The probe field is set to $E_1 = 0.2E_0$ and standard damping is used.

amplitudes (maintaining $E_1/E_0 = 0.2$) at fixed $g/J = 0.5$ and $g'/J' = 0.5$. While the area under the peaks depends quadratically on E_0 in both J - and J' -models, an approximately quadratic shift of the peak position is clear only in the J -model, where this effect is very strong [Figs. 13(a) and 13(c)]. In the J' -model, it may be possible to discern a very weak quadratic variation of the peak positions with E_0 , but there are clearly other contributions to their shift from the band edge.

In Fig. 14 we vary the spin damping, finding a minor broadening of the resonance peaks in line with general expectations. The reduction of the peak shifts with increasing γ_s are at first sight less intuitive, but results from the fact that the total response of the spin system is reduced by stronger damping, as already observed in the stationary phonon displacements, \bar{q}_0 and \bar{q}'_0 , shown in Fig. 10.

Finally, in Fig. 15 we vary the probe amplitude. Again we consider both J - and J' -models, but only the $\omega_0 = 2.2J$ phonon, in order to compare the situation with no pump field, $E_0 = 0$, to standard driving. Applied alone [Figs. 15(a) and 15(b)], the weak probe field changes neither the position nor the width of the resonance peak, and only its height depends quadratically on E_1 . However, the peak appears with an additional shift, which we denote simply by $\delta\omega_s$ in each panel of Fig. 15, that results from the weak hybridization of the band-edge states with a phonon whose frequency lies well inside the band. Quite generally, such a shift appears at both ends of the spectrum of the spin-phonon system at equilibrium, as the hybridization assures the addition of a single mode, such that both band edges are shifted outwards. When the phonon frequency is far from the band edges, the band-edge states can be regarded as $s < 1$ analogs of the phonon-bitripleton of Sec. IV, but as ω_0 is moved systematically towards one or

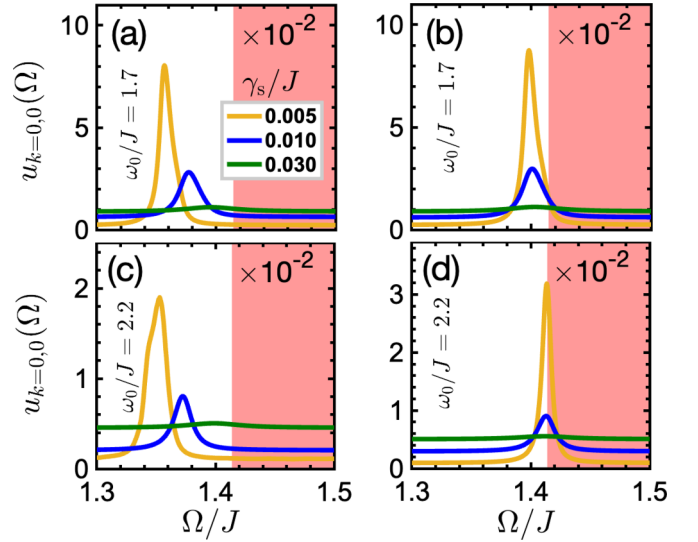


FIG. 14. Dependence of pump-probe protocol on spin damping. Average value of $u_{k=0}$, shown as a function of the probe frequency Ω around the lower band edge of [(a),(c)] a J -model and [(b),(d)] a J' -model with $g/J = 0.5 = g'/J'$ for different values of the spin damping γ_s . Standard driving is applied at $\omega = \omega_0 = 1.7J$ in panels (a) and (b) and at $2.2J$ in panels (c) and (d). The probe field is set to $E_1 = 0.2E_0$ and standard phonon damping is used.

other band edge then a true phonon-bitripleton would form at this edge. The probe field is added to provide the weak driving at band-edge frequencies that is required for a detailed characterization of the equilibrium and nonequilibrium response (meaning without and with E_0). We comment that the hybridization effect leading to $\delta\omega_s$ is very similar in the J - and J' -models, as may be expected given the relevant matrix elements, which are gy'_k and $-g'y'_k/\lambda$. This weak frequency shift is readily accounted for in order to quantify accurately the band-engineering effects produced by applying the pump field [Figs. 15(c) and 15(d)].

Figure 16(a) illustrates, using the example of the upper band edge in a J -model, the three effects contributing to the positions of the resonance peaks detected in the pump-probe protocol. It is clear that the first-order shift, which we denote $\delta\omega_{\max}^{(1)}$, is largest in absolute value, and is negative (Sec. V A). The next effect by magnitude is the hybridization shift, $\delta\omega_s$, which is positive at the upper band edge. However, analyzing the computed peak positions reveals that these two contributions are not sufficient for an accurate description, whereas the small discrepancy is well accounted for by $\delta\omega_{\max}^{(2)}$.

Figures 16(b) and 16(c) represent the relative signs and sizes of these three contributions at both band edges in the J -model, comparing them with an equivalent J' -model for two different phonon frequencies. Here we introduce additional, self-explanatory notation to distinguish the hybridization shifts of both models at both band edges. This format makes clear that $\delta\omega^{(1)}$ is the largest shift and is always downwards, whereas $\delta\omega^{(1)}$ is smaller and can change sign with the location of the driving phonon in the lower or upper half of the band. By contrast, $\delta\omega_s$ and $\delta\omega^{(2)}$ are always similar to $\delta\omega'_s$ and $\delta\omega^{(2)}$, and have the same (opposing) signs in all cases. We remark again that the quantitative results are similar

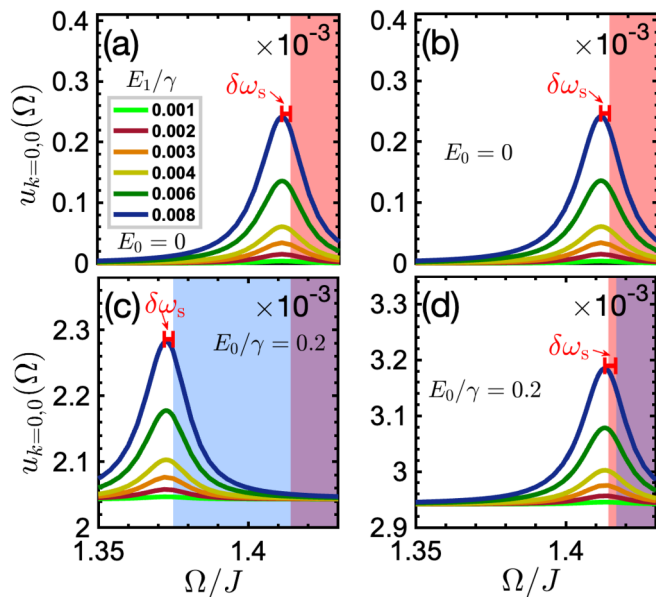


FIG. 15. Dependence of pump-probe protocol on probe amplitude. Average value of $u_{k=0}$, shown as a function of the probe frequency Ω around the lower band edge of [(a),(c)] a J -model and [(b),(d)] a J' -model with $g/J = 0.5 = g'/J'$ for different probe amplitudes E_1 . A phonon of frequency $\omega_0 = 2.2J$ is present. The pump field is set to zero in panels (a) and (b) and to standard driving at $\omega = 2.2J$ in panels (c) and (d). Standard damping is used. The red (light gray) shading represents the frequency range of the equilibrium two-tripion band (i.e., in the absence of driving), the blue (medium gray) shading the driving-renormalized band, and the purple color (dark gray shading) their superposition. $\delta\omega_s$ denotes a constant (E_1 -independent) shift of the observed peak from the equilibrium [(a),(b)] and nonequilibrium [(c),(d)] band edges, which arises due to weak hybridization ($s < 1$) of the band-edge two-tripion modes with the in-band phonon, and thus is directed away from the band center.

for the upper and lower band edges, which is why we have analyzed $u_{k=\pi,0}$ and $u_{k=0,0}$ interchangeably, instead of doubling the length of our discussion. We remark once more that only $\delta\omega^{(1)}$ and $\delta\omega^{(2)}$ are consequences of the magnetophononic driving, whereas $\delta\omega_s$ is an equilibrium effect of spin-phonon hybridization.

For complementary insight into our pump-probe results, in Fig. 17(a) we show the phonon spectrum $n_{\text{ph0}}(\omega_0, \Omega)$ matching the spin response of Fig. 15(c), i.e., for probe frequencies around the lower band edge, and in Fig. 17(b) the phononic response for probing around the upper band edge. In the absence of a probe beam, the phonon occupation is essentially flat around the band edges, with no discernible features forming in these regions when the only driving is resonant with the available in-band phonon at $\omega_0 = 2.2J$. However, increasing the probe intensity reveals that the formation of the predominantly magnetic spectral features at the band edge in Figs. 12–15 is accompanied by a small dip in $n_{\text{ph0}}(\omega_0, \Omega)$. This weak response indicates the weak phononic character of these hybrid states; the fact that it is negative is a consequence of the removal of phonon energy required in the excitation of the band-edge hybrid.

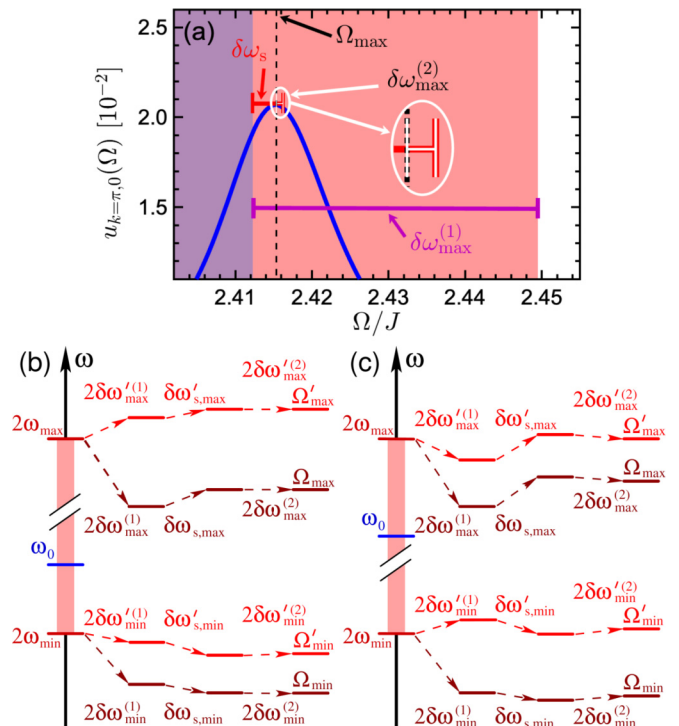


FIG. 16. Three frequency shifts in driven spin chains. Representation of the frequency shifts contributing to the positions of resonance peaks measured by scanning the probe frequency Ω . (a) Frequency shifts at the upper band edge, shown by considering the occupation, $u_{k=\pi,0}$, of $k = \pi$ triplon modes as a function of Ω for a J -model with $g = 0.5J$, $E_0/\gamma = 0.2$, $E_1 = 0.2E_0$, and $\omega_0 = 2.2J$. The horizontal bars and arrows quantify the contributions $\delta\omega_{\text{max}}^{(1)}$, $\delta\omega_{\text{max}}^{(2)}$, and $\delta\omega_s$. Ω_{max} indicates the probe frequency at which the resonance peak is observed. (b) Schematic vertical representation of the three frequency shifts at both band edges for a J -model (dark red or gray) and a J' -model (light red or gray) driven by a phonon whose frequency lies in the lower half of the two-tripion band. (c) Equivalent representation of frequency shifts for J - and J' -models driven by a phonon whose frequency lies in the upper half of the band. Panels (b) and (c) provide a qualitative comparison of the signs and sizes of the three shifts in each case, but are not drawn precisely to scale.

We conclude our analysis of spin-band engineering by stressing that our focus has been to illustrate all of the qualitative phenomena present when pumping with a light-driven phonon and probing with a separate laser in the same frequency range. For this purpose we have not considered the effects of the phonon coordinate on the magnetic interactions beyond linear order. We have also not dwelled on maximizing the energy shifts we induce, and thus we have shown mostly percent effects. However, we comment that the band shifts exceeding 10% that are found at stronger pump fields (Fig. 13) can for a one-dimensional system mean that well over 50% of the spin spectral weight is shifted completely out of its previous energy range. In the present study we have also used a rather generic spin band, whose gap is approximately equal to its band width, whereas focusing on a particularly narrow-band system would lead to much stronger relative shifts of spectral weight.

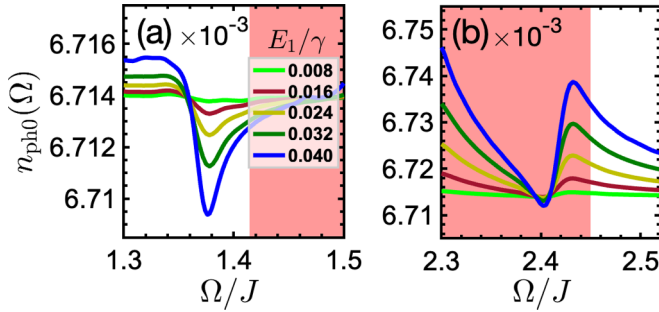


FIG. 17. Phononic response in the pump-probe protocol. (a) Phononic occupation $n_{\text{ph}0}$ shown as a function of the probe frequency Ω around (a) the lower and (b) the upper band edge of a J -model with $g/J = 0.5$ for different probe amplitudes, E_1 , when standard driving at $\omega = \omega_0 = 2.2J$ and standard damping are applied. We draw attention to the scales of the two y axes.

VI. STRONG SPIN-PHONON COUPLING IN QUANTUM MAGNETIC MATERIALS

A. CuGeO₃

The strong spin-phonon coupling in CuGeO₃ was revealed by the fact that it drives a spin-Peierls transition at $T_{\text{sp}} = 14$ K [27]. While it is clear that the leading physics of this system is a dimerization of the spin chain formed by the strongest (Cu-O-Cu) superexchange bonds, details of the magnon dispersion and of other thermodynamic measurements led to the introduction of both a significant next-neighbor coupling J_2 , and a non-negligible interchain coupling. A recent ultrafast investigation that used soft x-ray frequencies to probe the low-lying electronic states [23] also suggested that the observed damping was a consequence of coherently excited phonon modes coupling strongly to short-ranged magnetic correlations.

The crystal structure of CuGeO₃ has space group $Pmma$, which is reduced to $Cmca$ when the spin-Peierls transition enlarges the unit cell (while maintaining the orthorhombic symmetry). IR-active phonons are available over a wide range of energies in the high-temperature structure [29], and the rather large unit cell of the spin-Peierls phase makes their number significant, although for laser-driving purposes we note that all of the A_u modes are silent. Inelastic neutron scattering (INS) has been used to characterize all the phonon modes of the high-temperature phase [32,34], finding the strongest response at frequencies of 3.2 and 6.8 THz, and suggesting that the spin-Peierls transition is of a type occurring without an accompanying soft mode [59,60]. Here we comment that ultrafast methods appear to offer a qualitatively different approach to the investigation of low-lying phonons around and below the spin-Peierls temperature [61]. In Fig. 18 we illustrate three phonon modes of the high-temperature structure that have been identified by comparing electronic structure calculations [61] with experiment [29]. One of these [Fig. 18(a)] is IR-silent whereas the other two are expected to be promising candidates for coherent laser driving. We note also that most of these phonon modes tend to involve motions of all the atoms in the system, and hence they will have both J - and J' -model character in the language of our two simplifying models (Fig. 1).

The magnetic excitation spectrum, also measured by INS [30], shows relatively broad triplon bands, by which is meant that their gap is considerably smaller than their band width. In Figs. 19(a) and 19(b) we show the one-triplon dispersion along and across the chain direction, from which the early two-dimensional fit of Ref. [31] deduced the illustrative superexchange parameters $J = 10.7$ meV, which sets the one-triplon band center, $J' = 8.3$ meV (i.e., $\lambda = 0.78$), $J_2 = 0$, and $J_a = 1.5$ meV (interchain); we remark here that later studies provided a more refined global parameter set [62]. Figure 19(c) represents the full energy range of the two-triplon excitation spectrum for these parameters and also shows the in-band locations of four IR-symmetric phonon modes of the high-temperature structure, as measured by Ref. [29]. As noted above, the A_u mode [Fig. 18(a)] is IR-silent, but the B_{1u} , B_{2u} , and B_{3u} modes all have similar oscillator strengths [29]. We therefore propose the B_{1u} mode shown in Fig. 18(b) as a good candidate for driving in the lower half of the two-triplon band and the B_{3u} mode of Fig. 18(c) as a good candidate for driving in the upper half of the band, while we do not show the atomic motions in the B_{2u} mode because it is rather close to the two-triplon band center. We stress that, because ultrafast driving experiments are also performed with ultra-intense electric fields, the choice of drivable phonons is by no means restricted to the modes depicted in Fig. 19, and our qualitative message is rather that CuGeO₃ remains an excellent candidate material for observing the phenomena we analyze (Secs. III, IV, and V). However, we note also that the relevant experiments do need to be performed at low temperatures, $T \ll T_{\text{sp}} = 14$ K, in order to preserve the dimerized state of the system.

B. (VO)₂P₂O₇

As a low-dimensional $S = 1/2$ quantum spin system with an excitation gap, (VO)₂P₂O₇ first attracted attention as a candidate to realize the two-leg ladder geometry. However, INS measurements of the triplon dispersion [35] soon revealed its nature as a quasi-one-dimensional alternating spin chain, and nuclear magnetic resonance (NMR) revealed a large and complex structural unit cell with alternation in all three lattice directions [63]. Further theoretical analysis then deduced the presence of frustrated interchain coupling, leading to a magnetic model containing two species of dimerized spin chain, lying on alternating planes and with an effective coupling that is weak as a consequence of interchain frustration [36]. For experimental purposes, the intrinsic dimerization of the dominant spin chains avoids the need for temperatures as low as those required in CuGeO₃.

The crystal structure of (VO)₂P₂O₇ also has orthorhombic symmetry, with space group $Pca2_1$, and a very large unit cell (104 atoms). This structure lacks inversion symmetry, and hence all of the phonons may have either IR or Raman character, depending on the polarization of the light. Thus an extremely large number of IR-active phonons is available over the full range of energies. Initial studies of the phonon spectrum by Raman scattering [28] found by raising the temperature that a very strong renormalization of the phonons by the spin sector takes place. Theoretical fits [36] suggested that the spin-phonon coupling should be very strong, $g \simeq 0.5J$,

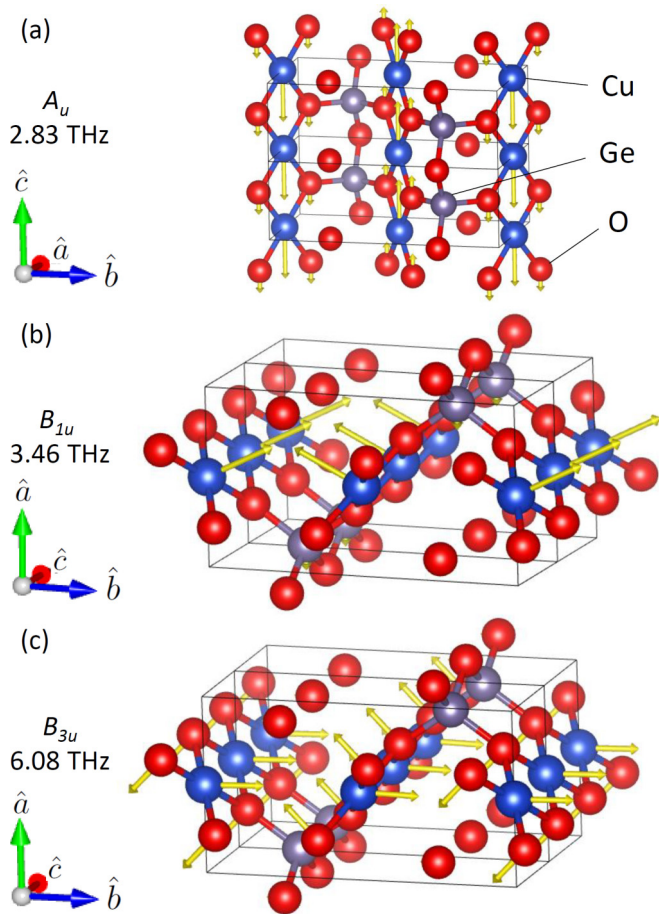


FIG. 18. Selected phonon modes in CuGeO_3 . Representation of the atomic displacements (arrows) in three phonon excitations of the spin-Peierls phase of CuGeO_3 . The alternating (CuO_2) spin chains are oriented along the \hat{c} axis and the phonon symmetries and frequencies correspond to those identified in Refs. [29,34]. While the A_u mode (a) is silent to IR excitation, the B_{1u} (b) and B_{3u} modes (c) are expected to be readily driven by strong electric fields.

which was the basis for our extending the analyses of Secs. III, IV, and V to this value of g and g' .

Figure 20 shows the atomic displacements in three phonon excitations with relatively large oscillator strengths, which were found in exploratory electronic structure calculations of $(\text{VO})_2\text{P}_2\text{O}_7$ [66]. These calculations used Quantum Espresso [64] to obtain a stable and insulating structural solution by assuming antiferromagnetic order, but were neither optimized for correlation effects on the V ions nor compared to any experiments. Nonetheless, they do illustrate the key features of (i) a very large number of phonon modes and (ii) a general increase in the average oscillator strength of these phonons with frequency, arising because modes with larger dipole moments are stiffer. Despite the significant quantitative mismatch in frequencies, it is not unrealistic to suggest that the 121 cm^{-1} (3.63 THz) B_1 mode shown in Fig. 20(a) and the 167 cm^{-1} (5.01 THz) B_1 mode shown in Fig. 20(b), which has a weaker A_1 partner at 162 cm^{-1} (4.85 THz) in the calculation, are candidates for the 70 and 123 cm^{-1} modes [2.10 and 3.69 THz , the latter with a partner at 118 cm^{-1} (3.54 THz)] that appear

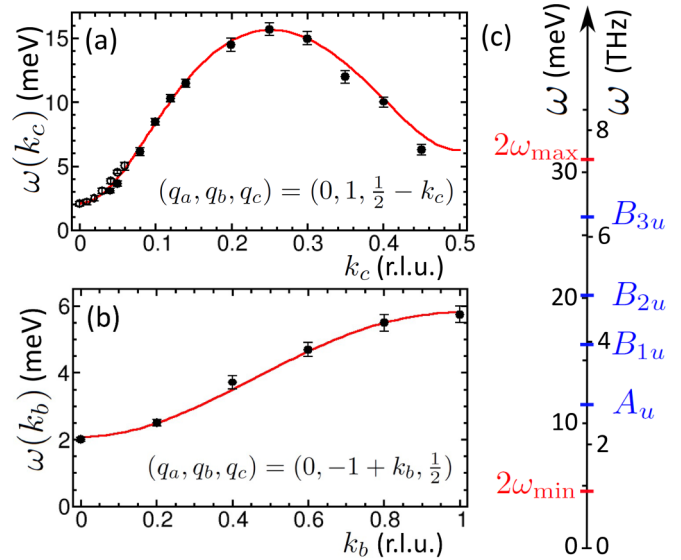


FIG. 19. One- and two-triplon spectra of CuGeO_3 . (a) Triplon dispersion along the chain direction (\hat{c}) in the spin-Peierls phase of CuGeO_3 . (b) Interchain (\hat{b}) triplon dispersion. Data in both panels were taken from Ref. [30] and fits from Ref. [31]. (c) Extrema, $2\omega_{\min}$ and $2\omega_{\max}$, of the two-triplon spectrum of CuGeO_3 at low temperatures, showing the locations of the four phonon modes, including the three depicted in Fig. 18.

most strongly in experiment [28]. One may anticipate that these two modes are the most suitable low-frequency candidates for coherent laser driving, but we stress again that many suitable modes are present at higher frequencies, including the 212 cm^{-1} (6.35 THz) A_1 mode shown in Fig. 20(c).

Following the fit of Ref. [36], Figs. 21(a) and 21(b) show the one-triplon dispersions along and across the direction of the alternating chains in the two inequivalent planes (which we denote A and B). Again both triplon bands are broad, with gaps rather smaller than their band widths [35], and with fitting parameters $J_A = 12.3\text{ meV}$, $J'_A = 8.1\text{ meV}$ (i.e., $\lambda_A = 0.66$), $J_{aA} = 1.0\text{ meV}$, $J_{bA} = 1.4\text{ meV}$ (the latter pair mutually frustrating interchain interactions) and $J_B = 10.4\text{ meV}$, $J'_B = 8.0\text{ meV}$ (i.e., $\lambda_B = 0.77$), $J_{aB} = 1.1\text{ meV}$, $J_{bB} = 1.6\text{ meV}$. Figure 21(c) represents the full energy range of the two two-triplon excitation spectra, assuming only processes involving pairs of A and pairs of B triplons, and again shows the locations of the three phonons whose normal modes are displayed in Fig. 20. We conclude that $(\text{VO})_2\text{P}_2\text{O}_7$ should offer an excellent materials platform for realizing all three of the magnetophononic phenomena revealed in our study.

C. Ultrafast band-engineering experiments

Experiments designed to follow the theoretical protocol of creating true spin NESS, at frequencies resonant with the spin spectrum and in bulk-driven quantum magnets, require a thin-film geometry and very efficient thermal transfer in order to maintain a low sample temperature [24]. In principle, self-blocking allows some relaxation of the constraints on pump intensity, driving time, and sample thickness, although in practice strong electromagnetic driving can induce heating by a variety of channels. An ultrafast pulsed protocol avoids

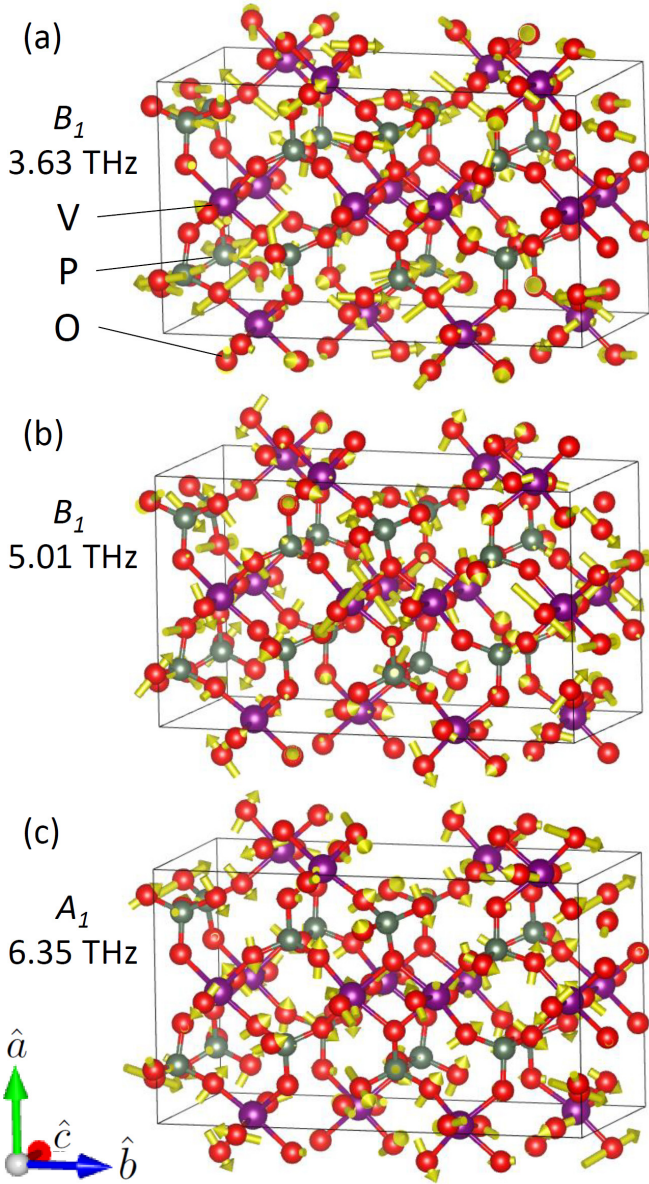


FIG. 20. Selected phonon modes in $(\text{VO})_2\text{P}_2\text{O}_7$. Representation of the atomic displacements (arrows) in three phonon excitations of the $(\text{VO})_2\text{P}_2\text{O}_7$ lattice. The dimerized spin chains are oriented along the \hat{b} axis and the frustrated interchain bonds lie in the ab plane. The normal modes illustrated are three examples with larger oscillator strengths found in a lattice-dynamics calculation performed using PHONOPY and based on density-functional-theory calculations performed with Quantum Espresso [64].

extreme heating problems through the very short driving time, but usually involves strong electric fields and samples of μm up to mm thicknesses, and thus the pulse repetition time should remain long. In the context of modifying the spin excitation spectrum, we comment that $\tilde{J}(q_0)$ and $\tilde{J}'(q_0)$ are in general highly nonlinear functions of q_0 , and where conventional experimental probes usually require only a low-order expansion, coherent laser driving can produce very large q_0 values [22].

A final issue concerns the optimal type of experiment to perform. Coherent light remains a rather insensitive direct

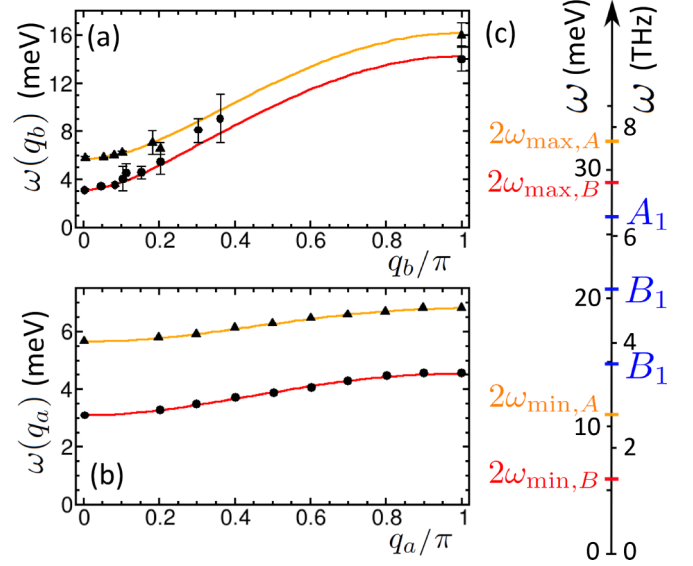


FIG. 21. One- and two-triplon spectra of $(\text{VO})_2\text{P}_2\text{O}_7$. (a) Dispersions of the two triplon branches along the chain direction (\hat{b}) in $(\text{VO})_2\text{P}_2\text{O}_7$. (b) Interchain (\hat{a}) triplon dispersions. Data in both panels were taken from Ref. [35], other than the zone-boundary points in panel (a), which were taken from Ref. [65]. The fits in both panels were taken from Ref. [36]. (c) Extrema, $2\omega_{\min,B}$ and $2\omega_{\max,A}$, of the two-triplon spectrum of $(\text{VO})_2\text{P}_2\text{O}_7$, showing the locations of the three phonon modes depicted in Fig. 20.

probe of magnetism, and experiments performed to date, such as absorption, reflection, and polarization rotation (birefringence), probe only some effects of the lattice that reflect the spin-phonon coupling. To identify other probes of novel magnetic states applicable to a complete analysis of a driven CuGeO_3 or $(\text{VO})_2\text{P}_2\text{O}_7$ system, we will continue to review the rapidly evolving technological developments in the measurement of quantities such as magnetic circular dichroism, the magneto-optic Kerr effect, or second-harmonic polarimetry as time-resolved variants become available across an increasing spectrum of probing frequencies (up to and including x-rays). The formalism of Sec. II remains fully applicable to the expectation values measured by these more direct probes of magnetic order, correlations, and excitations.

VII. DISCUSSIONS AND CONCLUSIONS

Ultrafast laser technology has enabled qualitative advances in the study of nonequilibrium phenomena in correlated condensed matter. Extending the reach of ultrafast driving methods to the rich variety of complex many-body states available in quantum magnetic materials requires overcoming the fact that the direct coupling of light to spin is generally rather weak, and thus inefficient. For this purpose we investigate the magnetophononic channel, in which the driving laser couples to an infrared-active optical phonon and the associated lattice displacements modulate the magnetic interactions. This approach offers highly frequency-specific driving possibilities by exploiting the resonances both between laser and phonon and between the driven phonon and the excitations of the quantum spin system. Intense driving electric fields

and strong spin-phonon coupling then allow one to probe the properties of a correlated quantum magnet driven far from its equilibrium state.

The characteristic energy scales in quantum magnetic materials are typically rather low, making their quantum many-body states very sensitive to heating, as a result of which no serious analysis can avoid taking the energy flow into account. To model the problem of a quantum magnet with both driving and dissipation through the lattice phonons, we adopt the Lindblad treatment of open quantum systems and analyze the nonequilibrium stationary state (NESS) of system subjected to continuous laser driving. Within this framework we consider a very straightforward example of a gapped spin system, the dimerized spin chain, whose elementary excitations are triplons that can be treated as conventional (rather than hard-core) bosons for sufficiently strong dimerization. We adopt a similarly minimal model for the driven phonon, namely an infrared-active optical mode coupled to only to the strong bonds (J -model) or only to the weak bonds (J' -model) of the dimerized chain.

Having previously used this minimal magnetophononic model to establish the framework for the weak-coupling, or linear-response, regime of the J -model [24], the primary focus of our present study is the regime of strong feedback, or back action, of the driven spin system on the driving phonon. Particularly when the phonon frequency is chosen close to the band edges of the two-spin excitation spectrum, a strong spin-phonon coupling causes strong hybridization into composite collective states whose characteristic frequencies differ significantly from those of their constituents. In the model we study, these collective states are phonon-bitriplons, a somewhat rare example of a composite formed from three bosons of two different types.

In a NESS experiment, the shift of characteristic frequencies causes a dramatic “self-blocking” effect, by which the spin system acts as a strong negative feedback on the driven phonon. This self-blocking is a manifestation of an intrinsic property of a magnetophononic system, in that the level repulsion caused by spin-phonon hybridization pushes the phonon resonance off a driving frequency selected to match the bare phonon spectrum, drastically suppressing the effective driving field. Only in an experiment with a range of driving frequencies, such as those present in an ultrashort pulse, would one observe the shifts of spectral weight associated with the multilevel repulsion occurring between the driven phonon and the macroscopic number of triplon pairs. Even in this situation, however, the self-blocking caused by strong mixing with off-resonant spin levels remains significant. We comment here that our present study retained the NESS protocol for all possible driving frequencies, and did not include the intense and instantaneous nature of an ultrashort pulse.

While driving phonons resonant with the two-spin band edges is an excellent way to create composite collective hybrid states, an important consequence of self-blocking is that it is not a very efficient way to engineer the bulk properties of a quantum magnet. Optical control is the only technique available to switch these properties on the characteristic timescales of the spin system, and our analysis reveals the important insight that the frequencies most efficient for this purpose lie in specific regions within the two-spin excitation

spectrum. The dominant band-engineering effects arise at linear order as a consequence of a stationary displacement of the driven phonon, which results from the steady population of excited triplons created by its action on the spin system. While the second-order contribution is weak, it is also detectable for the typical parameters of a phonon-driven quantum magnet, and thus is required for a quantitative description of experiment. To detect spin-band engineering, we introduce a weak “probe” beam, which in the NESS protocol is actually a further continuous driving term, applied in addition to the pump but at a completely independent frequency. (We remind the reader that the focus of our present study is not on conventional pump-probe physics, where a time delay between the pump and probe pulses is used to investigate transient phenomena at switch-on.) This technique yields clear additional signals in the phonon and spin response at the band-edge frequencies of the renormalized, or optically engineered, band. Applying a band-edge probe electric field to a system with a driven mid-band phonon reveals an extra intrinsic frequency shift in the detected signal, caused by off-resonant spin-phonon hybridization, that should also be included in any quantitative analysis.

Our minimal quantum magnetic model contains only two types of bond, within (J) and between (J') the spin dimers, and coupling the driven phonon to each bond type separately yields some valuable insight. Certain aspects of the response, which with strong spin-phonon coupling is dominated by the feedback between the two sectors, are very similar, in particular the self-blocking and the formation of composite collective states at the band edges. This can be traced to the fact that the matrix elements for the driven phonon to create spin excitation are the same, up to a sign, when the relative couplings (g/J and g'/J') are the same. By contrast, the band-engineering effect of the driven phonon is completely different between the two situations, which is a consequence of how the back action from the spin system modifies the phonon. Only in the J -model does the driving produce a rather large stationary shift of the equilibrium atomic displacement, whereas in the J' -model this effect is at least an order of magnitude weaker; once again this behavior can be traced to the matrix elements in the relevant equations of motion. Although it is easy to conclude that phonons coupling to the strong bonds are better suited for spin-band engineering, in fact the difference is also qualitative, in that modulating the intradimer bond changes the band center whereas modulating the bonds between dimers can be used to alter the band width. Although the effect on the band center is always a reduction, the band width can be renormalized both upwards or downwards by choosing the frequency of the driving phonon.

In the present paper we have focused on a spin chain as a representative quantum magnet. However, the generic features of the phenomenology we unveil are not restricted to spin chains, and could also be found in spin ladders and in valence-bond states in two and three dimensions. One important ingredient of our model is the presence of sharp peaks in the density of states at both band edges, which concentrates the strongest response of the spin system to two narrow ranges of frequency, and this property can be found in many quantum magnets with a spin gap or with narrow bands, such as those induced by frustrated couplings. Even for magnetically

ordered states in three dimensions, there is a large jump in the density of states at the upper band edge [14]. Band engineering, which relies on mid-band rather than band-edge phonons, is less dependent on the structure of the density of states, and is a more direct consequence of strong spin-phonon coupling at the strongest bonds of the system. The concept of phononic driving is of course applicable throughout condensed matter, and future work in quantum magnetism can be expected to investigate its manifestations in itinerant as well as in localized systems, in ordered as well as in nonordered magnets, and in systems with the wealth of complex forms of order found only in magnetic materials, including $3Q$ textures, quadrupolar order, chiral order, nematic order, and still others.

Here we have restricted our considerations to linear magnetophononics, in that we consider only a single driven phonon to explore the leading nonequilibrium phenomena. At this level, the dominant effects are produced by the q_0 -linear correction to the magnetic interactions, and we do not consider higher-order terms in $J(q_0)$ [the second-order correction we discuss appears in $q(t)$, generated by the equations of motion]. Nonlinear magnetophononics [22] considers the simultaneous effects of two or more driving phonons, and in this situation the quadratic correction to $J(q_a, q_b)$ contains terms modulating the magnetic interactions at frequencies of $2\omega_a$, $2\omega_b$, $\omega_a + \omega_b$, and $\omega_a - \omega_b$. The sum and difference frequencies enlarge very considerably the range of possibilities available for matching the driving frequency to the characteristic energies of the spin system. In particular, phonon difference frequencies are the key to magnetophononic driving in systems where the spin energy scale is very small, which is the situation relevant to a high percentage of quantum magnetic materials. Observing the signals of such nonlinear driving require one or both of strong spin-phonon coupling and ultra-intense electric fields.

Finally, we have discussed two materials matching our models, to show that the phenomena we identify should be detectable in CuGeO_3 and especially in $(\text{VO})_2\text{P}_2\text{O}_7$.

However, a primary task of theoretical physics is to build models matching the materials on which experiments are performed. For this task, the minimal magnetophononic model we have constructed is extremely versatile, in that more complex spin systems (for example higher-dimensional, ordered, or with anisotropic interactions), more complex phonons (for example dispersive, multiple, or coupling to both J and J' bonds), and also more complex dissipative processes (in particular spin-conserving ones) are readily accommodated within the Lindblad formulation to generate qualitatively similar equations of motion. As noted above, although we have considered only the expectation values of the most fundamental phonon and triplon operators, all more complex observables are formed from these and hence our framework is easily adapted to compute the quantities probed by experiment, and in particular those obtained from direct optical probes of magnetic correlations.

ACKNOWLEDGMENTS

We are indebted to N. Colonna, S. Das, and L. Spitz for performing DFT and phonon spectrum calculations, and for their assistance in producing Figs. 18 and 20. We thank S. Behrensmeier for assistance with Figs. 19 and 21, and M. Assmann, F. B. Anders, D. Bossini, K. Deltenre, F. Giorgianni, Ch. Rüegg, L. Spitz, and R. Valentí for helpful discussions. We are grateful to the German Research Foundation (DFG) for financial support through Projects No. UH 90-13/1 and No. B8 of ICRC 160, as well as to the Mercator Research Center Ruhr for support through the Mercur Kooperation Ko-2021-0027. We acknowledge the National Science Foundation for financial support through Awards No. MPS-2228725, No. DMR-1945529, No. PHY-1607611, and No. PHY-1748958 and the Welch Foundation for support through Award No. AT-2036-20200401. This project was partially funded by The University of Texas at Dallas Office of Research and Innovation through the SPIRe program.

-
- [1] P. Salén, M. Basini, S. Bonetti, J. Hebling, M. Krasilnikov, A. Y. Nikitin, G. Shamuilov, Z. Tibai, V. Zhaunerchyk, and V. Goryashko, Matter manipulation with extreme terahertz light: Progress in the enabling THz technology, *Phys. Rep.* **836-837**, 1 (2019).
 - [2] T. Kampfrath, K. Tanaka, and K. A. Nelson, Resonant and nonresonant control over matter and light by intense terahertz transients, *Nat. Photon* **7**, 680 (2013).
 - [3] X. C. Zhang, A. Shkurinov, and Y. Zhang, Extreme terahertz science, *Nat. Photon* **11**, 16 (2017).
 - [4] M. Buzzi, M. Först, R. Mankowsky, and A. Cavalleri, Probing dynamics in quantum materials with femtosecond x-rays, *Nat. Rev. Mater.* **3**, 299 (2018).
 - [5] T. Oka and S. Kitamura, Floquet engineering of quantum materials, *Annu. Rev. Condens. Matter Phys.* **10**, 387 (2019).
 - [6] A. Cavalleri, Photo-induced superconductivity, *Contemp. Phys.* **59**, 31 (2018).
 - [7] S. Iwai, M. Ono, A. Maeda, H. Matsuzaki, H. Kishida, H. Okamoto, and Y. Tokura, Ultrafast Optical Switching to a Metallic State by Photoinduced Mott Transition in a Halogen-Bridged Nickel-Chain Compound, *Phys. Rev. Lett.* **91**, 057401 (2003).
 - [8] A. de la Torre, D. M. Kennes, M. Claassen, S. Gerber, J. W. McIver, and M. A. Sentef, Colloquium: Nonthermal pathways to ultrafast control in quantum materials, *Rev. Mod. Phys.* **93**, 041002 (2021).
 - [9] T. Kampfrath, A. Sell, G. Klatt, A. Pashkin, S. Mährlein, T. Dekorsy, M. Wolf, M. Fiebig, A. Leitenstorfer, and R. Huber, Coherent terahertz control of antiferromagnetic spin waves, *Nat. Photon* **5**, 31 (2011).
 - [10] R. V. Mikhaylovskiy, E. Hendry, A. Secchi, J. H. Mentink, M. Eckstein, A. Wu, R. V. Pisarev, V. V. Kruglyak, M. I. Katsnelson, T. Rasing, and A. V. Kimel, Ultrafast optical modification of exchange interactions in iron oxides, *Nat. Commun.* **6**, 8190 (2015).

- [11] M. Jäckl, V. I. Belotelov, I. A. Akimov, I. V. Savochkin, D. R. Yakovlev, A. K. Zvezdin, and M. Bayer, Magnon Accumulation by Clocked Laser Excitation as Source of Long-Range Spin Waves in Transparent Magnetic Films, *Phys. Rev. X* **7**, 021009 (2017).
- [12] A. S. Disa, M. Fechner, T. F. Nova, B. Liu, M. Först, D. Prabhakaran, P. G. Radaelli, and A. Cavalleri, Polarizing an antiferromagnet by optical engineering of the crystal field, *Nat. Phys.* **16**, 937 (2020).
- [13] D. Afanasiev, J. R. Hortensius, B. A. Ivanov, A. Sasani, E. Bousquet, Y. M. Blanter, R. V. Mikhaylovskiy, A. V. Kimel, and A. D. Caviglia, Ultrafast control of magnetic interactions via light-driven phonons, *Nat. Mater.* **20**, 607 (2021).
- [14] K. Deltenre, D. Bossini, F. B. Anders, and G. S. Uhrig, Lattice-driven femtosecond magnon dynamics in α -MnTe, *Phys. Rev. B* **104**, 184419 (2021).
- [15] D. Bossini, S. Dal Conte, M. Terschanski, G. Springholz, A. Bonanni, K. Deltenre, F. Anders, G. S. Uhrig, G. Cerullo, and M. Cinchetti, Femtosecond phononic coupling to both spins and charges in a room-temperature antiferromagnetic semiconductor, *Phys. Rev. B* **104**, 224424 (2021).
- [16] A. S. Disa, T. F. Nova, B. Liu, and A. Cavalleri, Engineering crystal structures with light, *Nat. Phys.* **17**, 1087 (2021).
- [17] M. Först, C. Manzoni, S. Kaiser, Y. Tomioka, Y. Tokura, R. Merlin, and A. Cavalleri, Nonlinear phononics as an ultrafast route to lattice control, *Nat. Phys.* **7**, 854 (2011).
- [18] A. Subedi, A. Cavalleri, and A. Georges, Theory of nonlinear phononics for coherent light control of solids, *Phys. Rev. B* **89**, 220301(R) (2014).
- [19] A. von Hoegen, R. Mankowsky, M. Fechner, M. Först, and A. Cavalleri, Probing the interatomic potential of solids with strong-field nonlinear phononics, *Nature (London)* **555**, 79 (2018).
- [20] T. F. Nova, A. Cartella, A. Cantaluppi, M. Först, D. Bossini, R. V. Mikhaylovskiy, A. V. Kimel, R. Merlin, and A. Cavalleri, An effective magnetic field from optically driven phonons, *Nat. Phys.* **13**, 132 (2017).
- [21] M. Fechner, A. Sukhov, L. Chotorlishvili, C. Kenel, J. Berakdar, and N. A. Spaldin, Magnetophononics: Ultrafast spin control through the lattice, *Phys. Rev. Mater.* **2**, 064401 (2018).
- [22] F. Giorgianni, B. Wehinger, S. Allenspach, N. Colonna, C. Vicario, P. Puphal, E. Pomjakushina, B. Normand, and C. Rüegg, Ultrafast frustration-breaking and magnetophononic driving of singlet excitations in a quantum magnet, [arXiv:2101.01189](https://arxiv.org/abs/2101.01189).
- [23] E. Paris, C. W. Nicholson, S. Johnston, Y. Tseng, M. Rumo, G. Coslovich, S. Zohar, M. F. Lin, V. N. Strocov, R. Saint-Martin *et al.*, Probing the interplay between lattice dynamics and short-range magnetic correlations in CuGeO₃ with femtosecond RIXS, *npj Quantum Mater.* **6**, 51 (2021).
- [24] M. Yarmohammadi, C. Meyer, B. Fauseweh, B. Normand, and G. S. Uhrig, Dynamical properties of a driven dissipative dimerized $S = 1/2$ chain, *Phys. Rev. B* **103**, 045132 (2021).
- [25] G. Lindblad, On the generators of quantum dynamical semigroups, *Commun. Math. Phys.* **48**, 119 (1976).
- [26] H.-P. Breuer and F. Petruccione, *The Theory of Open Quantum Systems* (Clarendon Press, Oxford, 2006).
- [27] M. Hase, I. Terasaki, and K. Uchinokura, Observation of the Spin-Peierls Transition in Linear Cu²⁺ (Spin- $\frac{1}{2}$) Chains in an Inorganic Compound CuGeO₃, *Phys. Rev. Lett.* **70**, 3651 (1993).
- [28] M. Grove, P. Lemmens, G. Güntherodt, B. C. Sales, F. Büllsfeld, and W. Assmus, Magnetoelastic coupling and spin excitations in the spin-gap system (VO)₂P₂O₇: A Raman scattering study, *Phys. Rev. B* **61**, 6126 (2000).
- [29] Z. V. Popović, S. D. Dević, V. N. Popov, G. Dhahlenne, and A. Revcolevschi, Phonons in CuGeO₃ studied using polarized far-infrared and Raman-scattering spectroscopies, *Phys. Rev. B* **52**, 4185 (1995).
- [30] L. P. Regnault, M. Aïn, B. Hennion, G. Dhahlenne, and A. Revcolevschi, Inelastic neutron scattering investigation of the spin-Peierls system CuGeO₃, *Phys. Rev. B* **53**, 5579 (1996).
- [31] G. S. Uhrig, Symmetry and Dimension of the Dispersion of Inorganic Spin-Peierls Systems, *Phys. Rev. Lett.* **79**, 163 (1997).
- [32] M. Braden, B. Hennion, W. Reichardt, G. Dhahlenne, and A. Revcolevschi, Spin-Phonon Coupling in CuGeO₃, *Phys. Rev. Lett.* **80**, 3634 (1998).
- [33] R. Werner, C. Gros, and M. Braden, Microscopic spin-phonon coupling constants in CuGeO₃, *Phys. Rev. B* **59**, 14356 (1999).
- [34] M. Braden, W. Reichardt, B. Hennion, G. Dhahlenne, and A. Revcolevschi, Lattice dynamics of CuGeO₃: Inelastic neutron scattering and model calculations, *Phys. Rev. B* **66**, 214417 (2002).
- [35] A. W. Garrett, S. E. Nagler, D. A. Tennant, B. C. Sales, and T. Barnes, Magnetic Excitations in the $S = 1/2$ Alternating Chain Compound (VO)₂P₂O₇, *Phys. Rev. Lett.* **79**, 745 (1997).
- [36] G. S. Uhrig and B. Normand, Magnetic properties of (VO)₂P₂O₇: Two-plane structure and spin-phonon interactions, *Phys. Rev. B* **63**, 134418 (2001).
- [37] M. Yarmohammadi, Non-equilibrium dynamics of a driven-dissipative dimerized spin-1/2 chain, PhD Thesis, TU Dortmund, 2022.
- [38] S. Sachdev and R. N. Bhatt, Bond-operator representation of quantum spins: Mean-field theory of frustrated quantum Heisenberg antiferromagnets, *Phys. Rev. B* **41**, 9323 (1990).
- [39] B. Normand and C. Rüegg, Complete bond-operator theory of the two-chain spin ladder, *Phys. Rev. B* **83**, 054415 (2011).
- [40] C. Knetter and G. S. Uhrig, Perturbation theory by flow equations: dimerized and frustrated $S = 1/2$ chain, *Eur. Phys. J. B* **13**, 209 (2000).
- [41] K. P. Schmidt and G. S. Uhrig, Excitations in One-Dimensional $S = 1/2$ Quantum Antiferromagnets, *Phys. Rev. Lett.* **90**, 227204 (2003).
- [42] S. L. McCall and E. L. Hahn, Self-induced transparency, *Phys. Rev.* **183**, 457 (1969).
- [43] K. Huang, Lattice vibrations and optical waves in ionic crystals, *Nature (London)* **167**, 779 (1951).
- [44] S. Luo, H. Zhou, L. Zhang, and Z. Chen, Nanophotonics of microcavity exciton-polaritons, *Appl. Phys. Rev.* **10**, 011316 (2023).
- [45] D. N. Basov, A. Asenjo-Garcia, P. J. Schluck, X. Zhu, and A. Rubio, Polariton panorama, *Nanophotonics* **10**, 549 (2021).
- [46] Special issue on Jaynes-Cummings physics *J. Phys. B: At. Mol. Opt. Phys.* **46**, 220201–224025 (2013).
- [47] C. Berk, M. Jaris, W. Yang, S. Dhuey, S. Cabrini, and H. Schmidt, Strongly coupled magnon-phonon dynamics in a single nanomagnet, *Nat. Commun.* **10**, 2652 (2019).

- [48] M. Harder and C.-M. Hu, Cavity spintronics: An early review of recent progress in the study of magnon-photon level repulsion, *Solid State Phys.* **69**, 47 (2018).
- [49] S. Toth, B. Wehinger, K. Rolfs, T. Birol, U. Stuhr, H. T. amd K. Kimura, T. Kimura, H. M. Rønnow, and C. Rüegg, Electromagnon dispersion probed by inelastic x-ray scattering in LiCrO₂, *Nat. Commun.* **7**, 13547 (2016).
- [50] J. Lorenzana and G. A. Sawatzky, Phonon Assisted Multimagnon Optical Absorption and Long Lived Two-Magnon States in Undoped Lamellar Copper Oxides, *Phys. Rev. Lett.* **74**, 1867 (1995).
- [51] J. Lorenzana and G. A. Sawatzky, Theory of phonon-assisted multimagnon optical absorption and bimagnon states in quantum antiferromagnets, *Phys. Rev. B* **52**, 9576 (1995).
- [52] M. Grüninger, D. van der Marel, A. Damascelli, A. Erb, T. Nunner, and T. Kopp, Midinfrared absorption in YBa₂Cu₃O₆: Evidence for a failure of spin-wave theory for spin 1/2 in two dimensions, *Phys. Rev. B* **62**, 12422 (2000).
- [53] M. Windt, M. Grüninger, T. Nunner, C. Knetter, K. P. Schmidt, G. S. Uhrig, T. Kopp, A. Freimuth, U. Ammerahl, B. Büchner, and A. Revcolevschi, Observation of Two-Magnon Bound States in the Two-Leg Ladders of (Ca, La)₁₄Cu₂₄O₄₁, *Phys. Rev. Lett.* **87**, 127002 (2001).
- [54] D. A. Bozhko, V. I. Vasyuchka, A. V. Chumak, and A. A. Serga, Magnon-phonon interactions in magnon spintronics, *Low Temp. Phys.* **46**, 383 (2020).
- [55] A. Eckardt, Atomic quantum gases in periodically driven optical lattices, *Rev. Mod. Phys.* **89**, 011004 (2017).
- [56] W. Buchmüller and C. Lüdeling, in *Proceedings of the European School of High-Energy Physics 2005*, edited by R. Fleischer (CERN Yellow Report, Geneva, 2006), Vol. 014, Chap. 6.
- [57] The CMS Collaboration, Measurements of properties of the Higgs boson decaying to a W boson pair in pp collisions at $\sqrt{s} = 13$ TeV, *Phys. Lett. B* **791**, 96 (2019).
- [58] S. Blanes, F. Casas, J. A. Oteo, and J. Ros, The Magnus expansion and some of its applications, *Phys. Rep.* **470**, 151 (2009).
- [59] C. Gros and R. Werner, Dynamics of the Peierls-active phonon modes in CuGeO₃, *Phys. Rev. B* **58**, R14677 (1998).
- [60] J.-P. Pouget, Microscopic interactions in CuGeO₃ and organic spin-Peierls systems deduced from their pretransitional lattice fluctuations, *Eur. Phys. J. B* **20**, 321 (2001).
- [61] L. Spitz, F. Giorgianni, N. Hua, E. Paris, C. Nicholson, C. Monney, B. Normand, C. Svetina, E. Razzoli, L. Patthey, T. Schmitt, and C. Rüegg, THz-driven manipulation of magnetoelectric dynamics in a spin-Peierls system (unpublished).
- [62] C. Knetter and G. S. Uhrig, Triplet dispersion in CuGeO₃: Perturbative analysis, *Phys. Rev. B* **63**, 094401 (2001).
- [63] J. Kikuchi, K. Motoya, T. Yamauchi, and Y. Ueda, Coexistence of double alternating antiferromagnetic chains in (VO)₂P₂O₇: NMR study, *Phys. Rev. B* **60**, 6731 (1999).
- [64] P. Giannozzi, Jr., O. Andreussi, T. Brumme, O. Bunau, M. B. Nardelli, M. Calandra, R. Car, C. Cavazzoni, D. Ceresoli, M. Cococcioni *et al.*, Advanced capabilities for materials modelling with Quantum ESPRESSO, *J. Phys.: Condens. Matter* **29**, 465901 (2017).
- [65] H. Schwenk, Dimerisierte Spinketten (Dimerized spin chains), Ph.D. thesis, Universität Frankfurt, 2000.
- [66] N. Colonna (private communication).
- Correction:* Support information in the Acknowledgment section was incomplete and has been fixed.